

Measuring Asteroid Rotation Periods Using the KMTNet Bulge Survey Data

Haitao Huang,¹ Hongjing Yang,^{1,2} Chung-Uk Lee,³ Bin Li,^{4,5} Qiyue Qian,⁶ Jun Tian,⁴ Tianjun Gan,^{7,8,1} Shude Mao,¹ Weicheng Zang,¹ and Dong-Jin Kim³

¹Department of Astronomy, Westlake University, Hangzhou 310030, Zhejiang Province, China

²Westlake Institute for Advanced Study, Hangzhou 310030, Zhejiang Province, China

³Korea Astronomy and Space Science Institute, Daejeon 34055, Republic of Korea

⁴CAS Key Laboratory of Planetary Sciences, Purple Mountain Observatory, Chinese Academy of Sciences, Nanjing 210008, China

⁵University of Science and Technology of China, Hefei 230026, China

⁶Department of Astronomy, Tsinghua University, Beijing 100084, China

⁷Instituto de Astrofísica de Canarias (IAC), Vía Láctea s/n, E-38205 La Laguna, Tenerife, Spain

⁸Dept. Astrofísica, Universidad de La Laguna (ULL), E-38206 La Laguna, Tenerife, Spain

ABSTRACT

Since 2015, the Korea Microlensing Telescope Network (KMTNet) has conducted high-cadence, near-continuous observations of the Galactic bulge for nearly nine months each year from three sites in Chile, South Africa, and Australia, and its wide field of view provides a unique opportunity to extract asteroid lightcurves from archival survey data. In this work, we performed photometric measurements of bright asteroids ($V < 20$ mag) identified within a one-square-degree field during the 2018 KMTNet bulge season. We derived reliable rotation periods for 96 asteroids, including 84 objects without previously published lightcurves. The reliable spin-rates of the asteroids in our sample are broadly consistent with those reported in the Asteroid Lightcurve Database. This archival mining approach can be readily extended to a much larger KMTNet footprint, and the existing ~ 12 deg² high-cadence KMTNet dataset has the potential to yield reliable rotation periods ($U \geq 2+$) for more than 5,500 asteroids, substantially expanding the current database of asteroid rotational properties.

1. INTRODUCTION

As of 16 May 2026, more than 1.54 million asteroids have been discovered according to the Jet Propulsion Laboratory (JPL) database¹. However, based on the most comprehensive photometric database of asteroids, the Asteroid Lightcurve Database² (LCDB; Warner et al. 2009), only 32,852 asteroids have lightcurve parameters published as of October 2023, corresponding to less than 2.2% of the currently known asteroid population (Xu et al. 2023). The asteroid lightcurves provide fundamental information about several physical properties of asteroids; for example, the rotation period can be measured from lightcurves (Harris et al. 1989; Yeh et al. 2020), the general shape can be estimated from the lightcurve amplitude (Pravec & Harris 2000; Lacerda & Luu 2003; Tian et al. 2022), the detailed shape model can be obtained from lightcurve inversion (Kaasalainen

et al. 1992a,b; Āurech et al. 2018), and the albedo can be roughly inferred from the phase-curve relation (Bowell et al. 1989). In addition, statistical distributions of asteroid spin-rates and pole orientations are essential for understanding how rotational states are influenced by multiple mechanisms, including collisional evolution, tidal interactions, internal structure, and the Yarkovsky–O’Keefe–Radzievskii–Paddack (YORP) effect (Vokrouhlicky et al. 2015; Pravec et al. 2008; Pravec & Harris 2000).

A fraction of the asteroid lightcurve parameters compiled in the LCDB were derived from targeted ground-based photometric observations using small- and medium-sized telescopes. Such efforts include the Small Main-Belt Asteroid Lightcurve Survey, which derived lightcurves for 32 small main-belt asteroids using the 1.8-m Perkins, 1.3-m McGraw–Hill, and 2.4-m Hiltner telescopes (Binzel et al. 1992), the Thousand Asteroid Light Curve Survey (TALCS), which measured lightcurves for 828 asteroids using the Canada–France–Hawaii Telescope (Masiero et al. 2009), and the EURONEAR Lightcurve Survey, which reported lightcurves for 101 near-Earth asteroids based on co-

Corresponding author: Hongjing Yang, Bin Li
hongjing.yang@qq.com, binli@pmo.ac.cn

¹ <https://ssd.jpl.nasa.gov/>

² <https://www.minorplanet.info/php/lcdb.php>

ordinated observations from 11 telescopes (Vaduvescu et al. 2017). With high cadence and high photometric precision, such observations enable the robust determination of asteroid rotation periods. However, because they typically focus on individual targets, only a limited number of asteroids can be monitored during a single observing night (Warner & Harris 2011).

In recent years, photometric data from several large time-domain surveys, originally not designed for asteroid studies, have increasingly been exploited for asteroid research and have significantly enlarged the lightcurve sample. Successful examples include the K2 mission of the Kepler Space Telescope, which obtained lightcurves for 608 main-belt asteroids and 10 Centaurs (Molnár et al. 2018; Marton et al. 2020), the Transiting Exoplanet Survey Satellite (TESS), which produced lightcurves for 17,189 asteroids (Pál et al. 2020; McNeill et al. 2019), the Palomar Transient Factory (PTF), which derived reliable rotation periods for more than 8,300 asteroids (Waszczak et al. 2015), the MOA-II microlensing survey, which derived 26 asteroid rotation periods (Cordwell et al. 2022), the Vera C. Rubin Observatory Legacy Survey of Space and Time (LSST), which derived lightcurves, rotation periods, and colors for approximately 2,000 asteroids (Greenstreet et al. 2026), and the European Space Agency Gaia mission, which provided unique spin-state solutions for more than 8,600 asteroids (Ďurech & Hanuš 2023). Together, these surveys have contributed tens of thousands of asteroid lightcurves and/or rotational solutions. Nevertheless, each of these surveys has its own observational limitations. For instance, although TESS provides high-cadence photometry, its relatively shallow limiting magnitude restricts the accessible asteroid population. Conversely, deep wide-field surveys such as the LSST will reach much fainter objects, but their nominal survey cadence is not generally optimized for detailed lightcurve characterization.

The Korea Microlensing Telescope Network (KMTNet) is a wide-field time-domain survey primarily designed for gravitational microlensing observations toward the Galactic bulge (Kim et al. 2016). The network consists of three identical 1.6-m telescopes, each equipped with a 4 deg² camera, located in Chile, South Africa, and Australia, enabling near-continuous monitoring of the same fields. With its typical deep limiting magnitude of approximately $V \sim 21$ mag (Lee et al. 2023) and high observational cadence (as short as 15 min for prime fields), KMTNet bulge observations are well suited for detecting and characterizing asteroid lightcurves.

In this work, we analyze the data from a one-square-degree KMTNet field during the 2018 bulge season and extract asteroid lightcurves from the difference images produced by Qian et al. (2025) using a “trailed” PSF photometry (see Sect. 3.2 for more details). While asteroid lightcurve photometry has previously been performed using KMTNet data obtained during the non-bulge observing seasons (Erasmus et al. 2017, 2018), this work presents the first systematic extraction of asteroid lightcurves from KMTNet bulge observations, where the crowding background present additional challenges for asteroid photometry.

The outline of the paper is as follows. Details of the telescope and our observations can be found in Section 2; the methodology of target selection, photometry, and lightcurve fitting is described in Section 3; the resulting asteroid period measurements are given in Section 4; and in Section 5 we summarize the results and discuss the expected yields from the KMTNet prime fields as well as future surveys.

2. OBSERVATIONS

KMTNet is a wide-field telescope network operated by the Korea Astronomy and Space Science Institute (KASI). The network comprises three identical 1.6-m telescopes equipped with a mosaic CCD camera consisting of four $9K \times 9K$ chips, providing a total field of view of 2.0×2.0 deg² with a pixel scale of $\sim 0.4''$. The three telescopes are located at the Cerro Tololo Inter-American Observatory (CTIO) in Chile, the South African Astronomical Observatory (SAAO) in South Africa, and the Siding Spring Observatory (SSO) in Australia. Owing to their longitudinal distribution across similar southern latitudes ($\sim -30^\circ$), the network enables near-continuous (24-hour) monitoring of targets in the Southern Hemisphere. KMTNet was designed primarily for microlensing surveys toward the Galactic bulge, which are conducted annually from mid-February to mid-October.

The KMTNet Galactic bulge survey began full operations in 2016, covering a total area of 96 deg². Within this region, about 12 deg² are designated as “prime” fields, observed with a cadence of 4 hr⁻¹ (i.e., one exposure every 15 minutes). The remaining fields are observed with cadences ranging from 1 hr⁻¹ to 0.2 hr⁻¹. Observations are primarily obtained in the Cousins I band, with $\sim 9\%$ of the images taken in the V band to enable color measurements. The exposure times of the I -band and V -band images are 60 s and 90 s, respectively. Although this observing strategy was originally optimized for detecting microlensing exoplanets, it is also well suited for asteroid lightcurve studies. For

typical main-belt asteroids with apparent motions of ~ 0.5 arcsec/min, the crossing time for a 1×1 deg² field is ~ 5 days. Consequently, a typical asteroid located in the prime field can be observed over ~ 10 days with up to $\sim 10^3$ exposures, making the bulge survey data a valuable resource for asteroid lightcurve measurements.

In this work, we utilize one-year *I*-band images from a ~ 1 deg² field centered at $(\alpha, \delta) = (269.22^\circ, -29.58^\circ)$ to explore the potential of KMTNet bulge data for asteroid lightcurve analysis (hereafter the target field). This area corresponds to the N CCD chip of the 02/42 bulge fields.

3. METHODOLOGY

3.1. Target Selection

To identify asteroids within the given KMTNet field during the 2018 observing season, we first query the Minor Planet Center (MPC) database³ for orbital elements. We exclude approximately 300,000 objects with poorly constrained orbital solutions, defined operationally as those with fewer than 30 reported observations in the MPC database, leaving about 1.2 million asteroids for further analysis. Ephemerides are then computed for these remaining objects at the times of each KMTNet exposure. For each exposure, we select asteroids whose predicted positions fall within the target field. For each selected asteroid, we record its pixel coordinates, on-sky position, orbital parameters, frame identifier, and the MPC-predicted *V*-band magnitude, phase angle, heliocentric distance, and geocentric distance. To ensure robust photometric measurements, we restrict our sample to asteroids with a sufficiently bright mean apparent magnitude, $V < 20$ mag. In total, 4,288 asteroids are expected to traverse the field during the season, of which 376 satisfy the magnitude criterion and are retained in the final sample. The final sample is dominated by main-belt asteroids, with typical ephemeris uncertainties of ~ 0.1 arcsec.

We perform photometry for all 376 asteroids. The distribution of their number of epochs is shown in Figure 1, with most asteroids having fewer than 300 observations.

3.2. Photometry

We perform photometric measurements based on the difference images generated by Qian et al. (2025). A difference image is obtained by subtracting a suitably convolved reference image from each science exposure. Specifically, the reference image for each field is constructed by stacking multiple high-quality exposures with 3σ clipping. Because asteroids move across exposures, their signals are removed during stacking, leaving

only stationary sources. The reference image is then convolved with a spatially varying kernel to match the PSF and sky background of the science exposure before subtraction (Bramich 2008; Albrow et al. 2009). Static sources are thus largely removed, while moving objects (asteroids) and transient signals remain. Residual stars in the difference images (e.g., in Figure 2) are primarily saturated stars and variable stars.

Asteroids move significantly during the 60 s exposure of KMTNet, causing their images to appear as trails rather than point-like sources. For a typical main-belt asteroid, the on-sky motion is approximately 0.5 arcsec per 60 s exposure. Given the KMTNet pixel scale of 0.4 arcsec pix⁻¹, this corresponds to a typical displacement of more than one pixel per exposure, indicating the necessity of a trailed PSF treatment.

To accurately extract fluxes for moving asteroids, we adopt a trailed PSF photometry approach on the difference images, extending the method described in Yang et al. (2023) by replacing the stationary PSF model with a trailed PSF model that accounts for the asteroid’s apparent motion during each exposure.

We model the two-dimensional intensity distribution of each exposure of each asteroid as a stationary PSF convolved with a linear kernel representing constant-velocity motion during the exposure. The stationary PSF for each image is derived from the reference image as part of the difference image pipeline (Qian et al. 2025). The asteroid’s position (x, y) is defined as its centroid at the midpoint of the exposure, and the linear motion kernel is constructed accordingly to represent the trail centered on this position. The trailed PSF model is then fitted to the difference image cutout for each exposure. The model includes parameters for the asteroid’s position (x, y) , flux f , and local (difference) background b . We minimize the χ^2

$$\chi^2(x, y, f, b) = \sum_{i,j} \frac{(\mathcal{D}_{i,j}^2 - f \cdot \mathcal{P}_{i,j}(x, y) - b)^2}{\sigma_{i,j}^2}, \quad (1)$$

to measure (x, y, f, b) , where $\mathcal{D}_{i,j}$ is the difference image pixel value at pixel (i, j) , $\mathcal{P}_{i,j}(x, y)$ is the pixelated trailed PSF model, and $\sigma_{i,j}$ is the pixel-wise uncertainty.

In principle, the measured flux f corresponds to the flux in the difference image. However, for an asteroid that is present in the science image but absent from the reference image (due to its motion), its entire signal appears in the difference image. Therefore, f directly represents the asteroid’s total flux.

To construct the trailed PSF model for each exposure, we first compute the asteroid’s instantaneous velocity from its orbital ephemeris. This initial velocity is used to build the linear motion kernel. We then perform the

³ <https://minorplanetcenter.net/iau/MPCORB.html>.

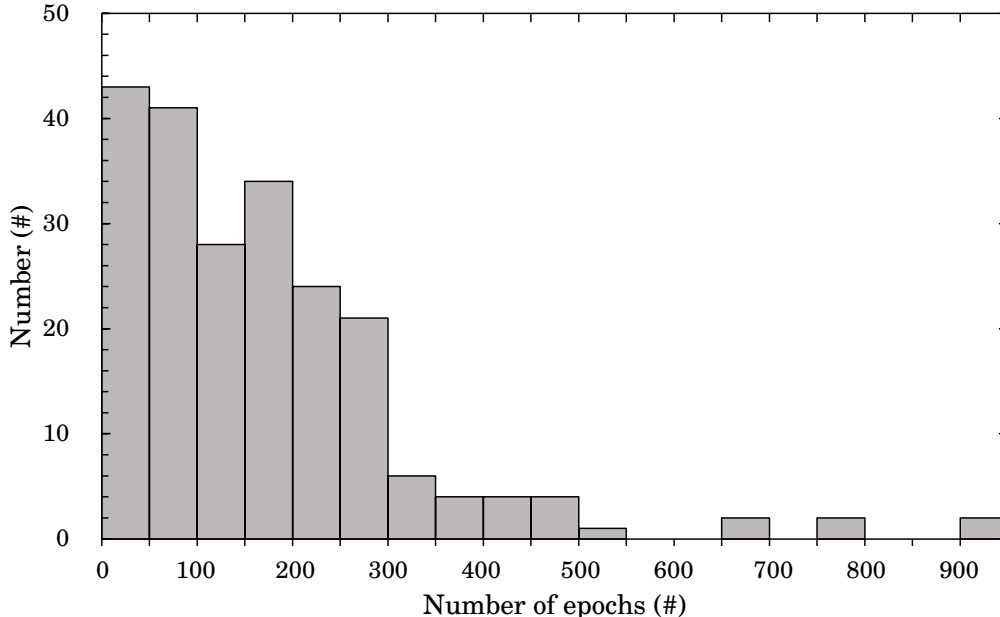


Figure 1. Distribution of Asteroid Observation Counts in the Pilot Dataset.

trailed PSF fitting for each exposure to obtain the position (x, y) and flux f . Using the fitted positions across multiple exposures within the same observational night, we refine the velocity estimate, update the motion kernel, and repeat the fitting process. This iterative procedure continues until the velocity converges, ensuring that the trailed PSF model accurately represents the asteroid’s motion.

Uncertainties in the fitted parameters are estimated following the method of Yang et al. (2023). For each measurement, we also derive a photometric quality indicator σ_{phot} (defined in Yang et al. 2023; Yang et al. 2025), which quantifies the goodness-of-fit and helps identify problematic measurements, such as those affected by saturated stars, bad columns, or other image artifacts.

Finally, the instrumental fluxes are converted to semi-calibrated magnitudes using a photometric zero point of $m_0 = 28.1$, determined from previous KMTNet observations.

$$m = m_0 - 2.5 \log_{10}(F), \quad (2)$$

where F is the instrumental flux. This conversion does not include detailed corrections (e.g., cross-matching to standard reference stars and measuring the actual zero point). However, this is sufficient because the primary goal of this study is to identify asteroid rotation periods, which are not sensitive to detailed photometric calibration.

As an example, Figure 2 illustrates the photometry procedure for asteroid (4362) Carlisle, showing from top to bottom: the original KMTNet SSO images, difference

images, zoomed cutouts of the difference images, residuals after subtracting the best-fit trailed PSF model, and the resulting lightcurve across five epochs. The clean residuals demonstrate the effectiveness of the trailed PSF photometry.

3.3. Lightcurve Analysis

3.3.1. Orbital Effect Correction

For each asteroid, to remove systematic brightness variations caused by changes in heliocentric distance, geocentric distance, and phase angle during the orbital motion, we apply distance and phase-angle corrections to each individual observation. After these corrections, the remaining magnitude variations—hereafter referred to as the “reduced magnitude”—primarily reflect the rotational modulation of the asteroid.

The magnitude of an asteroid can be described as

$$V = H + \delta + 5 \log_{10}(r\Delta) - 2.5 \log_{10}(\phi(\alpha)), \quad (3)$$

here, V corresponds to the apparent magnitude m defined in Eq.(2), where H is the absolute magnitude, r is the Sun-asteroid distance in A.U., Δ is the Earth-asteroid distance in A.U., δ describes the rotational and shape variation, and $\phi(\alpha)$ is the phase function, where α represents the phase angle, the angle between the Sun, the asteroid, and the Earth.

We model the phase function using the Lumme-Bowell model (Bowell et al. 1989), which is defined as

$$\phi = (1 - G)\phi_1 + G\phi_2, \quad (4)$$

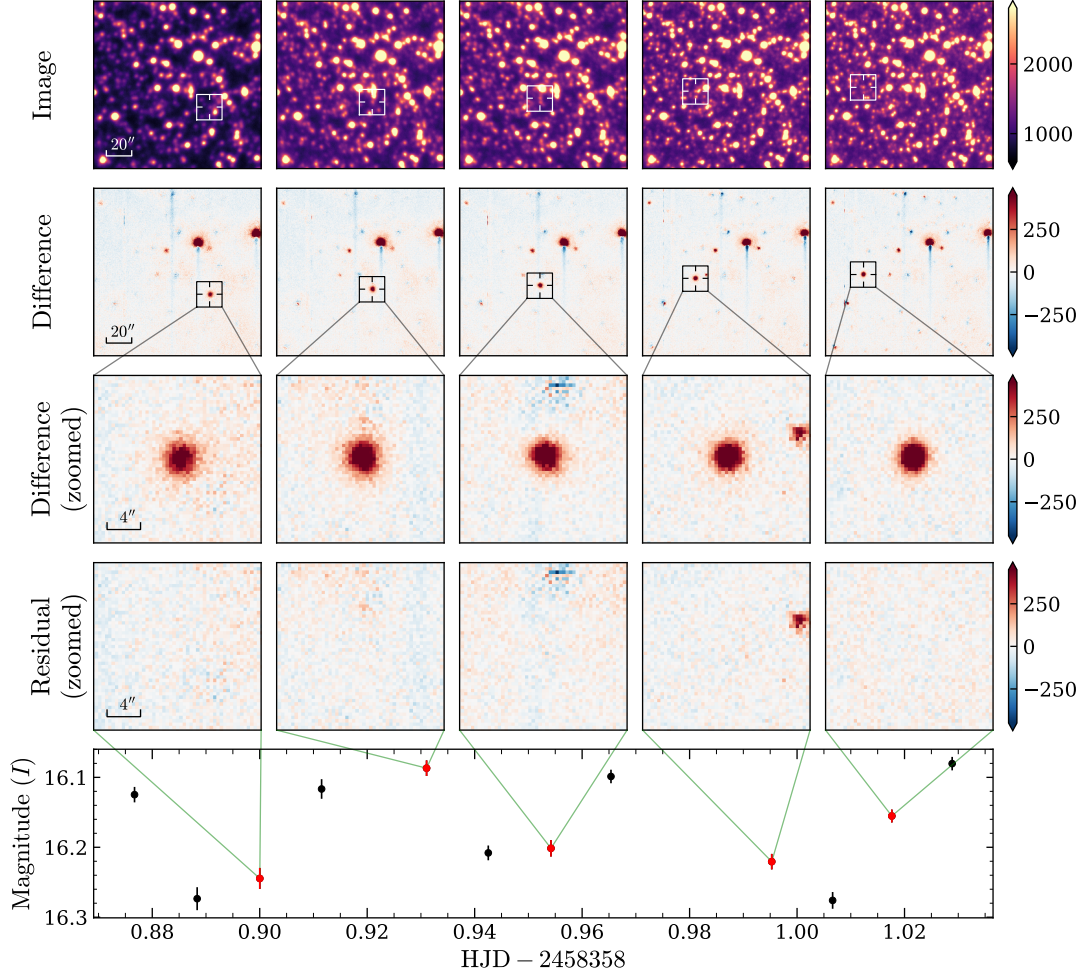


Figure 2. Illustration of the difference image and the trailed PSF photometry for asteroid (4362) Carlisle. Rows from top to bottom are: original KMTNet SSO images, difference images, zoomed cutouts of the difference images, residuals after subtracting the asteroid’s trailed PSF, and the resulting lightcurve, respectively. Columns from left to right show five different epochs. The asteroid (4362) Carlisle is marked in boxes in the top two rows. Fluxes are in instrumental units.

$$\phi_1 = \exp\left(-3.33 \tan^{0.63}\left(\frac{\alpha}{2}\right)\right), \quad (5)$$

$$\phi_2 = \exp\left(-1.87 \tan^{1.22}\left(\frac{\alpha}{2}\right)\right), \quad (6)$$

where the phase parameter G is fixed at 0.15.

3.3.2. Rotation Period Search

Before we proceed the period analysis, we first exclude poor photometric measurements. Data with negative flux, large ($> 3.4''$) or unphysically small seeing ($< 0.4''$), high sky background (> 5000 ADU), large positional uncertainty (≥ 2.5 pix or $1.0''$ in any direction), or bad image-subtraction quality (quality indicator $\sigma_{\text{subt}} > 1.7$; Yang et al. 2023) are excluded.

To determine the asteroid rotation period, we adopt a multi-stage procedure combining grid search, downhill refinement, and Markov Chain Monte Carlo (MCMC).

The lightcurve is modeled using a second-order Fourier series with coefficients a_0 , B_1 , B_2 , C_1 , and C_2 (Harris et al. 1989), which provides sufficient flexibility to reproduce the typical double-peaked morphology of asteroid rotational modulation. The model is expressed as

$$M_j = a_0 + \sum_{k=1,2}^{N_k} B_k \sin\left[\frac{2\pi k}{P}(t_j - t_0)\right] + \sum_{k=1,2}^{N_k} C_k \cos\left[\frac{2\pi k}{P}(t_j - t_0)\right], \quad (7)$$

where M_j is the I -band reduced magnitude (i.e., $H + \delta$ as defined in Eq. (3)) measured at epoch t_j ; t_j denotes the observation time of the j th data point; a_0 represents the mean magnitude level of the lightcurve, approximately corresponding to the absolute magnitude H ; B_k and C_k are the Fourier coefficients; P is the rotation period; and

t_0 is an arbitrary reference epoch. The present analysis assumes that the observed lightcurve is dominated by the rotational modulation of a single asteroid. Potential binary asteroid signatures, such as mutual events or additional periodic components, are not explicitly investigated in this work and will be addressed in a future study.

We first perform a period grid search over the range of 0.48–100 h with a uniform step of 0.01 h. The lower bound is chosen to be close to the Nyquist limit set by the typical cadence of ~ 15 min, below which period determinations may be affected by aliasing, corresponding to a spin frequency of 50 cycles per day. For each grid, the Fourier coefficients are determined via weighted least-squares fitting, and the goodness-of-fit is quantified using the χ^2 statistic, yielding a discrete $\chi^2(P)$ distribution. To improve robustness against outliers, the fitting procedure is iterated three times; after each of the first two iterations, data points deviating by more than 2σ from the model are rejected, and the fit is repeated on the remaining cleaned dataset.

Candidate periods are identified not only from the global minimum of the $\chi^2(P)$ distribution, but also from local minima satisfying $\Delta\chi^2 < 100$ relative to the global minimum. If no such solutions exist, the period corresponding to the second smallest χ^2 is adopted as a candidate. This selection accounts for the presence of aliasing (stroboscopic) effects caused by quasi-periodic sampling, which can produce multiple competing minima in χ^2 space. Retaining near-degenerate solutions prevents premature selection of an alias period at this stage (Pál et al. 2020). Even though KMTNet’s near-continuous coverage reduces diurnal-gap aliasing, we retain multiple candidate periods for each lightcurve at this stage to ensure robust period determination and avoid prematurely adopting an alias solution. For objects whose χ^2 distributions continued to decrease toward the upper boundary of the initial search range, the period search was manually extended beyond 100 h to identify additional candidate minima.

All candidate periods are subsequently refined using the Nelder–Mead simplex algorithm, jointly optimizing the period and Fourier coefficients to minimize χ^2 . The final best-fit period is chosen as the solution with the lowest χ^2 after refinement. The uncertainty of the derived period is then estimated using a Markov Chain Monte Carlo (MCMC) approach, sampling the joint posterior distribution of the period and Fourier coefficients. The reported period value and its uncertainty are the median and the (16%, 84%) percentiles of the marginalized posterior distribution.

Because asteroid lightcurves are generally expected to exhibit a double-peaked structure at the physical rotation frequency, we further examine the phase-folded light curves of candidate solutions via visual inspection. The adopted period produces a coherent and smooth double-peaked morphology with minimal scatter, whereas alternative (alias) solutions often yield less consistent phase-folded structures. If only a single peak is present, the solution at half the corresponding frequency is additionally evaluated by manually adjusting the trial period and re-examining the folded lightcurve, followed by the same optimization and uncertainty estimation procedure described above.

The final phase-folded lightcurve of each asteroid is then visually assigned a quality code “U”. According to the criteria of the LCDB, U = 3, 2, and 1 correspond to highly reliable, ambiguous, and low-reliability solutions, respectively. The updated system also allows ‘+’ and ‘−’ subdivisions, e.g., 2+ or 3, to refine the assessments even more (Warner et al. 2009). The resulting distribution of quality codes is as follows: 7, 29, 60, 40, 48, 74, and 118 asteroids are classified as U = 3, 3−, 2+, 2, 2−, 1+, and 1, respectively.

4. ASTEROID ROTATION PERIODS

4.1. Rotation Period and Quality

In total, 96 reliable rotation periods (i.e., $U \geq 2+$) are obtained, which are listed in Table 1, where only the first ten entries are shown. The complete table is provided in Appendix A. In addition to these reliable solutions, we also report less reliable rotation periods (i.e., $U < 2+$) for 123 asteroids in Appendix A, excluding asteroids for which no period could be determined due to insufficient data points.

Figure 3 shows an example of a folded lightcurve and normalised χ^2 distribution of the lowest numbered asteroid for which we found the period with U = 3. The folded lightcurves and normalized χ^2 distribution of the remaining U = 3 objects, as well as those with U = 3− and U = 2+, are available in Appendix B.

4.2. Comparison with LCDB and Individual Case

Among the 96 reliable rotation periods, 12 of them also have rotation periods published with $U \geq 2+$ in the LCDB. Table 2 shows a comparison of rotation periods for the 12 objects.

Most of the derived rotation periods are consistent with previously published results. One notable exception is asteroid (15699) Lytinen. In both datasets, the rotation period of this object is assigned a quality code of U = 2−, indicating a tentative but not fully reliable solution.

Table 1. List of reliable rotation periods (first 10 entries). The complete table is available in Appendix A.

Object	Period (h)	Quality	H^* (mag)	Magnitude (I-band)	Amplitude (mag)	Epochs	Phase Angle* ($^\circ$)
(1077) Campanula	3.8378 ± 0.0008	2+	12.36	15.407	0.4375	48	26.4939
(1152) Pawona	3.4348 ± 0.0004	2+	11.17	14.873	0.2216	83	24.4671
(1187) Afra	13.8938 ± 0.0119	2+	11.62	16.150	0.4563	47	21.0534
(1324) Knysna	2.5503 ± 0.0007	2+	13.20	15.548	0.1308	87	30.2324
(2294) Andronikov	3.1534 ± 0.0001	3-	11.91	14.925	0.4518	189	14.1802
(2438) Oleshko	3.2222 ± 0.0003	2+	13.02	15.660	0.2007	142	24.7712
(3180) Morgan	2.4481 ± 0.0004	3-	14.21	17.809	0.2003	200	22.0880
(3314) Beals	5.4650 ± 0.0039	2+	13.11	17.038	1.3315	24	23.7157
(4362) Carlisle	2.6320 ± 0.0002	2+	13.18	16.178	0.1878	170	24.5133
(5116) Korsor	4.5033 ± 0.0004	3	12.06	16.349	0.4812	114	2.2259

* Obtained from the MPCORB database.

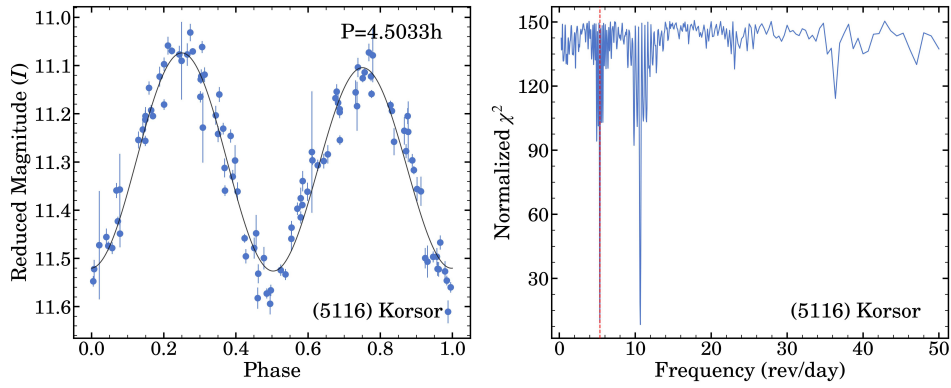


Figure 3. Folded lightcurve (left) and the normalized χ^2 distribution as a function of frequency (right) for asteroid with rotation-period quality code U = 3. Only the first panels are shown here to illustrate the format; the remaining panels are provided in Appendix B.

Table 2. Comparison of the Rotation Period for the 12 Objects having known LCDB measurements.

Object	Quality (this work)	LCDB period (h)	Our derived period (h)
(1077) Campanula	2+	3.8509	3.8378 ± 0.0008
(1152) Pawona	2+	3.4154	3.4348 ± 0.0004
(1187) Afra	2+	14.0701	13.8938 ± 0.0119
(1324) Knysna	2+	2.5538	2.5503 ± 0.0007
(2294) Andronikov	3-	3.1529	3.1534 ± 0.0001
(2438) Oleshko	2+	3.2270	3.2222 ± 0.0003
(3180) Morgan	3-	2.4477	2.4481 ± 0.0004
(3314) Beals	2+	5.4616	5.4650 ± 0.0039
(4362) Carlisle	2+	2.6329	2.6320 ± 0.0002
(5116) Korsor	3	4.5030	4.5033 ± 0.0004
(6399) Harada	3	11.0200	10.9662 ± 0.0002
(7284) 1989 VW	2+	26.4500	26.8283 ± 0.0549

In our data, the folded lightcurve of (15699) Lyytinen is characterized by a relatively small number of photometric measurements, and the data are noticeably scattered. This limited sampling is primarily due to the short time span during which the asteroid traverses the field of view, resulting in fewer observational epochs than ideal. The corresponding χ^2 -frequency distribution exhibits multiple local minima, leading to several competing candidate periods and making it difficult to uniquely identify a preferred solution. Based on these limitations, we conservatively assign a quality code of $U = 2$ to this object. Among the candidate solutions, the formally best-fit period is 2.3681 h, which is somewhat shorter than the previously reported LCDB value of 2.7818 h, and the associated uncertainty remains non-negligible (Figure 4).

The similarly low quality rating reported in the LCDB suggests that the ambiguity in the rotation period determination is not unique to our dataset, but may reflect an intrinsic difficulty in characterizing the rotational properties of this object. One possible explanation is that the asteroid exhibits a complex or non-principal axis rotation state (i.e., tumbling), which can produce irregular or non-periodic lightcurve variations that are not well described by a single-period model (Harris 1994; Pravec et al. 2005). Alternatively, the apparent ambiguity may arise from observational limitations, such as sparse temporal coverage or unfavorable viewing geometries, which can obscure or distort the underlying periodic signal (Harris et al. 1999).

Given the current data quality, it is not possible to unambiguously distinguish between these scenarios. However, the persistent difficulty in obtaining a stable and high-quality period solution for (15699) Lyytinen makes it a valuable target for follow-up observations. A denser and longer lightcurve coverage would be essential to confirm its rotational state and to determine whether its behavior is indeed indicative of more complex rotational dynamics.

In our sample, most ambiguous period determinations arise from insufficient photometric coverage of asteroids (typically fewer than 50 epochs), primarily due to limited observational epochs, with a minor contribution from data gaps caused by adverse weather conditions. When adequate coverage is available, our measured rotation periods are generally robust and reliable.

4.3. Statistical Properties

Figure 5 shows the distribution of the quality code as a function of the magnitude. The total number of asteroids exhibits a unimodal distribution, with a clear maximum in the 18–19 mag interval, where both high-

quality ($U \geq 2+$) and lower-quality ($U < 2+$) solutions reach their highest counts. Toward both brighter and fainter magnitudes, the number of objects decreases progressively. This behavior reflects the combined effects of the intrinsic asteroid brightness distribution and the observational selection function of our survey.

The decline toward brighter magnitudes is primarily driven by the intrinsic scarcity of large (and thus bright) asteroids. In contrast, the decrease at the faint end is largely a consequence of the magnitude-limited sample selection. Although our sample is selected with a limiting magnitude of $V \leq 20$, the use of the mean instrumental I -band magnitude introduces a systematic offset between the selection band and the analysis band. As a result, objects with I -band magnitudes in the range of 19–20 mag are underrepresented compared to those in the 18–19 mag bin.

The similar unimodal behavior observed in both the $U \geq 2+$ and $U < 2+$ subsamples indicates that the quality classification does not introduce a strong additional bias as a function of magnitude within the well-sampled range. Therefore, we suggest that our sample is broadly representative within the well-sampled magnitude range, providing a robust foundation for the subsequent statistical analysis of spin-rate properties. As shown in Figure 6, the reliable rotation periods derived from KMTNet observations span a wide range, from a few hours to over 100 h, with the shortest periods approaching the well-known spin barrier at ~ 2.2 h. This limit is generally interpreted as a consequence of the structural and compositional properties of asteroids, representing the critical rotation period beyond which gravitationally bound rubble-pile bodies would undergo rotational disruption (Dermott et al. 1984; Pravec & Harris 2000).

To further quantify the overall characteristics of this distribution, Figure 7 presents the spin-rate distribution of the asteroids in our sample and compares it with that reported in the LCDB. The primary horizontal axis shows the spin rate, while the secondary axis indicates the corresponding rotation period. The two distributions exhibit a generally consistent overall shape, with the majority of objects concentrated in the 1–5 rev/day range, broadly consistent with the well-established peak from previous studies. In terms of rotation period, most objects cluster between 6 and 12 h, and no objects with rotation periods shorter than ~ 2.2 h are found in our sample.

The absence of very fast rotators in our sample is likely primarily due to the magnitude-limited selection ($V \leq 20$), which biases the sample toward brighter and therefore typically larger asteroids that are less likely to

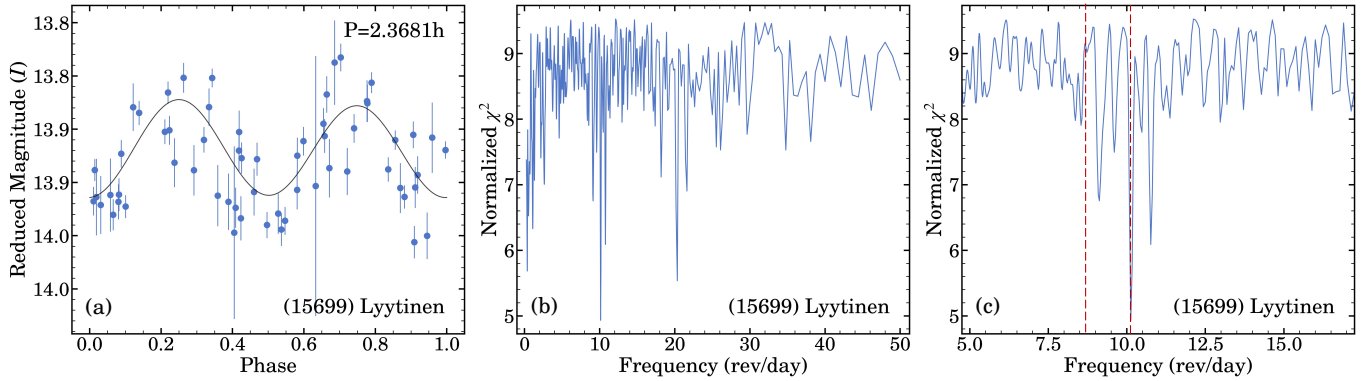


Figure 4. Phase-folded lightcurve and the normalized χ^2 distribution as a function of frequency for asteroid (15699) Lyytinen. Panel (a) shows the folded lightcurve, (b) presents the normalized χ^2 distribution as a function of frequency, and (c) is a zoom-in of panel (b) around the best-fit frequency. The two dashed lines indicate the LCDB (left) frequency and our measured period (right).

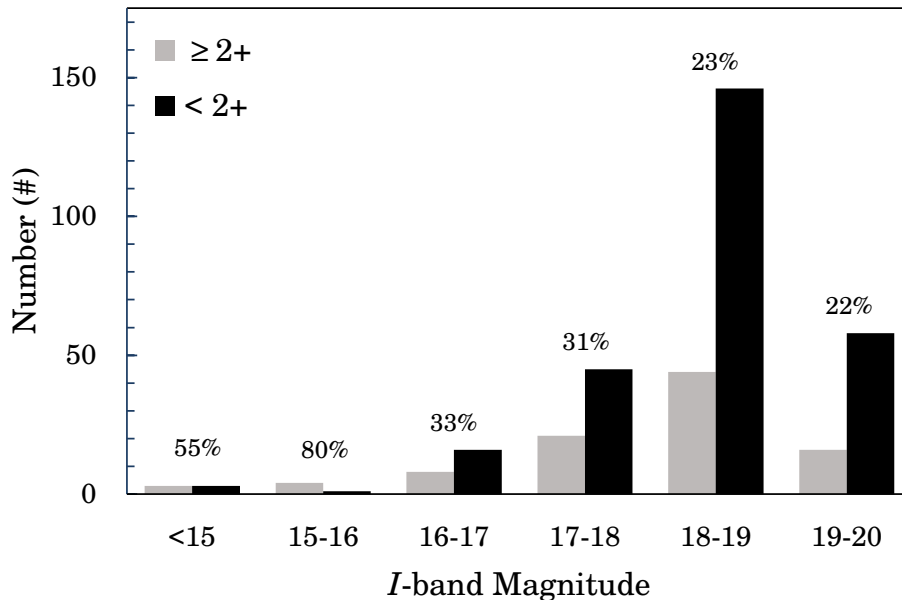


Figure 5. Asteroid number distribution of I -band magnitude, grouped in quality codes. The gray and black colors represent the rotation periods of $U \geq 2+$ and $U < 2+$ groups, respectively. The fraction listed above each magnitude bin indicates the fraction of $U \geq 2+$ objects.

exhibit extremely short rotation periods. Nevertheless, the near-continuous temporal coverage enabled by the multi-site observations of KMTNet, together with its photometric depth, suggests that extending the analysis to fainter targets and broader sky coverage should improve sensitivity to short-period rotators, potentially enabling the detection of objects approaching or even below the spin barrier. This interpretation is also supported by Figure 5, where the fraction of $U \geq 2+$ solutions does not show a sharp decline toward fainter mag-

nitudes, indicating that reliable period determinations remain achievable beyond the adopted sample limit.

We compared the period distributions of the reliable and less reliable samples. The latter have substantially longer periods (mean/median: 47.54/44.85 h) than the reliable sample (12.57/6.21 h), and also fewer observation epochs (134.0 vs. 176.4). We attribute this trend primarily to the limited field coverage (only one square degree): long-period asteroids may exit the field before sufficient rotational phase coverage is obtained, making their period determination less reliable. Furthermore,

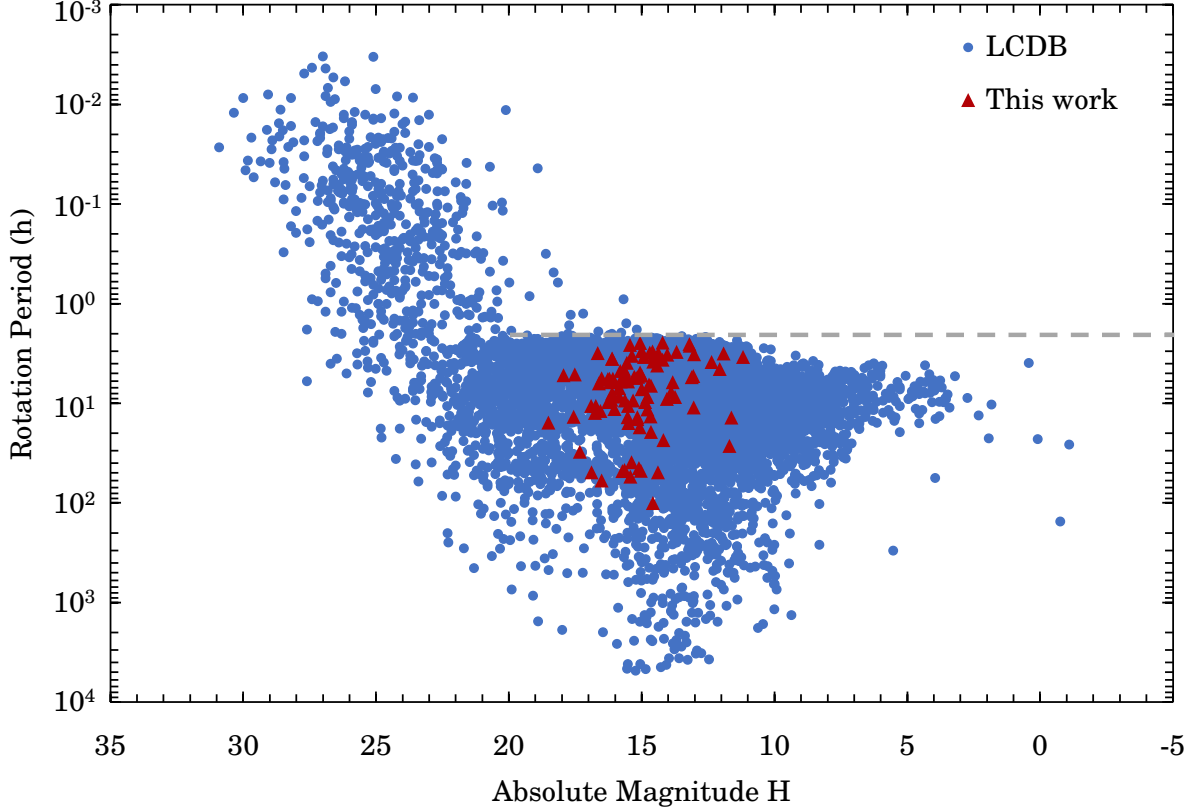


Figure 6. The magnitude–period two-dimensional distribution of asteroids with reliable rotation periods derived in this work, compared with those from the LCDB-BASIC (Warner et al. 2009). The gray dashed line indicates the asteroid spin barrier at ~ 2.2 h.

for those already classified as less reliable, the reported period values themselves may not be accurate. A future study over a larger area could help resolve this bias.

5. DISCUSSION AND CONCLUSION

5.1. Estimated Yields from the KMTNet Prime-Field Archive

To estimate the potential of the KMTNet archive for asteroid studies, we performed a systematic estimation of the number of asteroids traversing the ~ 12 deg² KMTNet ≥ 4 hr⁻¹ cadence prime fields (Kim et al. 2018) during the 2016–2025 period.

For each year, we considered an eight-month observing window from February 20 to October 20, corresponding to the typical Galactic bulge season. Representative observing epochs were adopted for each of the three KMTNet sites to approximate the temporal sampling: 02:30 and 06:30 UT for Chile, 12:30 and 14:30 UT for Australia, and 18:30 and 22:30 UT for South Africa. The analysis is restricted to the prime fields (Kim et al. 2018). For consistency in the yield estimation and to reflect the total discovery potential of KMTNet, asteroids identified within the 1 deg² pilot field analyzed in this

work (from the 2018 dataset) were not excluded from the calculation.

Based on the adopted observational sampling, we find that a total of 160,616 asteroids pass through the KMTNet fields over the considered time span. Applying a magnitude cut of $V \leq 21$, consistent with the expected photometric limit of KMTNet, yields 31,535 asteroids that are potentially detectable. Among these, 1,564 objects traverse the field more than once during this 10-year period, including 1,442 asteroids observed twice and 122 observed three times over the ten-year baseline.

In our sample, approximately 25% of the asteroids yield well-determined rotation periods ($U \geq 2+$). However, this recovery fraction is expected to decrease toward fainter magnitudes due to the lower signal-to-noise ratio and reduced lightcurve quality. Adopting a conservative recovery fraction of 20% for the full sample, we estimate that more than 6,300 asteroids could yield well-determined rotation periods. Among them, about 5,500 would be new measurements. This would represent a substantial increase compared to the current sample size of 8,998 objects with known rotation periods of quality code $U \geq 2+$ in the LCDB-BASIC (Figure 6),

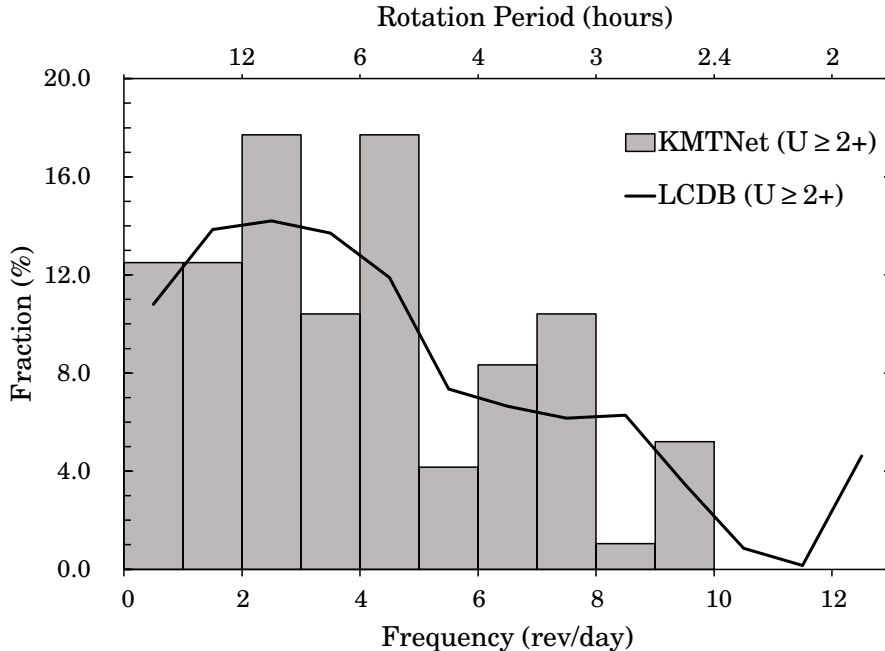


Figure 7. Density distribution of the asteroid spin frequency of $U \geq 2+$ asteroids derived from this work compared to that of the LCDB $U \geq 2+$ asteroids. The top axis showing the corresponding rotation period.

highlighting the considerable potential of the KMTNet archive for asteroid rotational studies.

In addition, asteroids that are observed over multiple seasons constitute a particularly valuable subsample. For these objects, the extended temporal baseline offers the opportunity to investigate potential variations in rotation period over timescales of several years, which may provide insights into rotational evolution processes such as the YORP effect or external perturbations.

5.2. Future Surveys

Future high-cadence time-domain surveys will further expand the potential of this approach. For example, the DECam Rogue Earths and Mars Survey (DREAMS) (Yang et al. 2026) employs the 3-deg² DECam instrument on the 4-m Blanco telescope and is observing the Galactic bulge field at minute-level cadence with substantially deeper photometric limits. The minute-cadence sampling makes it possible to detect and characterize very fast and super-fast rotators with rotation periods shorter than ~ 2.2 h, which are particularly important for constraining the internal structure and cohesion of small asteroids.

In addition, compared to KMTNet, the > 1.5 mag deeper limiting magnitude of DREAMS will enable the detection of significantly fainter objects, potentially extending asteroid lightcurve studies to $V \geq 22$. Given the steep increase in asteroid number counts toward fainter magnitudes, this capability may increase the accessible

sample size by orders of magnitude, further enriching the statistical sample of asteroid rotational properties.

Other large-scale surveys, such as the Vera C. Rubin Observatory Legacy Survey of Space and Time (LSST), will provide an important complementary capability. Although the nominal cadence of the main LSST survey is generally not optimized for detailed asteroid lightcurve characterization, recent high-cadence commissioning observations have demonstrated the strong potential of Rubin data for asteroid rotation studies (Greenstreet et al. 2026), particularly because of its substantially wider sky coverage and much larger asteroid sample compared with focused high-cadence surveys. Meanwhile, TESS offers stable high-cadence space-based photometry with nearly continuous temporal coverage, while KMTNet enables long-duration multi-site monitoring over consecutive nights. Together, these facilities provide highly complementary capabilities in cadence, depth, temporal coverage, and survey area.

In the future, combining datasets from multiple time-domain surveys will significantly improve the characterization of asteroid populations across a broad range of sizes and dynamical classes. The combination of high cadence, deep photometric limits, continuous monitoring, and ultra-wide sky coverage will not only enlarge the sample of asteroids with reliable rotational measurements, but also improve sensitivity to faint, fast-rotating, and previously unknown objects, thereby

enabling more comprehensive investigations of asteroid physical properties, rotational evolution, and the broader small-body population of the Solar System.

5.3. Summary

In this work, we show that KMTNet Galactic bulge observations can be effectively exploited to extract reliable rotation periods of asteroids, even within extremely crowded stellar fields toward the Galactic center. Using archival data from the 2018 bulge season and focusing on a one-square-degree field centered at $(\alpha, \delta) = (269.22^\circ, -29.58^\circ)$, we extract lightcurves for asteroids with $V < 20$ and derive 96 reliable rotation periods ($U \geq 2+$).

Among these, 84 asteroids have no previously published lightcurve information, representing a substantial addition to the existing sample, while the remaining 12 objects with previously reported periods in the LCDB show good agreement with our measurements. These results demonstrate that small bodies traversing dense stellar regions can be robustly detected and their photometric variations accurately characterized despite the challenging background conditions, highlighting the untapped potential of KMTNet bulge observations for Solar System studies.

Although based on a single pilot field, a systematic calculation based on the full KMTNet survey cadence, sky coverage, and multi-year baseline indicates that the archival dataset has the potential to yield ~ 5500 previously uncharacterized asteroids with reliable rotation periods, significantly expanding current rotation statistics.

H.H., H.Y., Q.Q., T.G., and S.M. acknowledge support by the National Natural Science Foundation of China (Grant No. 12133005). H.Y. acknowledge support by the China Postdoctoral Science Foundation (No. 2024M762938). The authors thank Dr. In-Gu Shin for helpful discussions regarding the KMTNet observations. This research has made use of the KMTNet system operated by the Korea Astronomy and Space Science Institute (KASI) at three host sites of CTIO in Chile, SAAO in South Africa, and SSO in Australia. Data transfer from the host site to KASI was supported by the Korea Research Environment Open NETwork (KREONET). This research was supported by KASI under the R&D program (project No. 2026-1-904-01) supervised by the Ministry of Science and ICT. The authors acknowledge the High-performance Computing center at Westlake University for providing computational and data storage resources that have contributed to the research results reported within this paper.

REFERENCES

- Albrow, M. D., Horne, K., Bramich, D. M., et al. 2009, *MNRAS*, 397, 2099, doi: [10.1111/j.1365-2966.2009.15098.x](https://doi.org/10.1111/j.1365-2966.2009.15098.x)
- Binzel, R. P., Xu, S., Bus, S. J., & Bowell, E. 1992, *Icarus*, 99, 225, doi: [https://doi.org/10.1016/0019-1035\(92\)90184-9](https://doi.org/10.1016/0019-1035(92)90184-9)
- Bowell, E., Hapke, B., Domingue, D., et al. 1989, *Asteroids II* (Tucson, AZ, Univ. Arizona Press)
- Bramich, D. M. 2008, *MNRAS*, 386, L77, doi: [10.1111/j.1745-3933.2008.00464.x](https://doi.org/10.1111/j.1745-3933.2008.00464.x)
- Cordwell, A. J., Rattenbury, N. J., Bannister, M. T., et al. 2022, *Monthly Notices of the Royal Astronomical Society*, 514, 3098, doi: [10.1093/mnras/stac674](https://doi.org/10.1093/mnras/stac674)
- Dermott, S. F., Harris, A. W., & Murray, C. D. 1984, *Icarus*, 57, 14, doi: [https://doi.org/10.1016/0019-1035\(84\)90003-4](https://doi.org/10.1016/0019-1035(84)90003-4)
- Đurech, J., & Hanuš, J. 2023, *Astronomy & Astrophysics*, 675, A24, doi: <https://doi.org/10.1051/0004-6361/202345889>
- Erasmus, N., McNeill, A., Mommert, M., et al. 2018, *The Astrophysical Journal Supplement Series*, 237, 19, doi: [10.3847/1538-4365/aac38f](https://doi.org/10.3847/1538-4365/aac38f)
- Erasmus, N., Mommert, M., Trilling, D. E., et al. 2017, *The Astronomical Journal*, 154, 162, doi: [10.3847/1538-3881/aa88be](https://doi.org/10.3847/1538-3881/aa88be)
- Greenstreet, S., Li, Z. C., Vavilov, D. E., et al. 2026, *The Astrophysical Journal Letters*, 996, L33, doi: [10.3847/2041-8213/ae2a30](https://doi.org/10.3847/2041-8213/ae2a30)
- Harris, A., Young, J., Bowell, E., & Tholen, D. 1999, *Icarus*, 142, 173, doi: <https://doi.org/10.1006/icar.1999.6181>
- Harris, A., Young, J., Bowell, E., et al. 1989, *Icarus*, 77, 171, doi: [https://doi.org/10.1016/0019-1035\(89\)90015-8](https://doi.org/10.1016/0019-1035(89)90015-8)
- Harris, A. W. 1994, *Icarus*, 107, 209, doi: <https://doi.org/10.1006/icar.1994.1017>
- Kaasalainen, M., Lamberg, L., & Lumme, K. 1992a, *Astronomy and Astrophysics* (ISSN 0004-6361), vol. 259, no. 1, p. 333-340., 259, 333
- Kaasalainen, M., Lamberg, L., Lumme, K., & Bowell, E. 1992b, *Astronomy and Astrophysics* (ISSN 0004-6361), vol. 259, no. 1, p. 318-332., 259, 318

- Kim, D.-J., Kim, H.-W., Hwang, K.-H., et al. 2018, *AJ*, 155, 76, doi: [10.3847/1538-3881/aaa47b](https://doi.org/10.3847/1538-3881/aaa47b)
- Kim, S.-L., Lee, C.-U., Park, B.-G., et al. 2016, *Journal of Korean Astronomical Society*, 49, 37, doi: [10.5303/JKAS.2016.49.1.37](https://doi.org/10.5303/JKAS.2016.49.1.37)
- Lacerda, P., & Luu, J. 2003, *Icarus*, 161, 174, doi: [https://doi.org/10.1016/S0019-1035\(02\)00019-2](https://doi.org/10.1016/S0019-1035(02)00019-2)
- Lee, H.-J., Kim, M.-J., Kim, D.-H., & Choi, Y.-J. 2023, in *LPI Contributions*, Vol. 2851, *Asteroids, Comets, Meteors Conference*, 2166
- Marton, G., Kiss, C., Molnár, L., et al. 2020, *Icarus*, 345, 113721, doi: <https://doi.org/10.1016/j.icarus.2020.113721>
- Masiero, J., Jedicke, R., Ďurech, J., et al. 2009, *Icarus*, 204, 145, doi: <https://doi.org/10.1016/j.icarus.2009.06.012>
- McNeill, A., Mommert, M., Trilling, D. E., Llama, J., & Skiff, B. 2019, *The Astrophysical Journal Supplement Series*, 245, 29, doi: [10.3847/1538-4365/ab5223](https://doi.org/10.3847/1538-4365/ab5223)
- Molnár, L., Pál, A., Sárneczky, K., et al. 2018, *The Astrophysical Journal Supplement Series*, 234, 37, doi: [10.3847/1538-4365/aaa1a1](https://doi.org/10.3847/1538-4365/aaa1a1)
- Pravec, P., & Harris, A. W. 2000, *Icarus*, 148, 12, doi: <https://doi.org/10.1006/icar.2000.6482>
- Pravec, P., Harris, A., Scheirich, P., et al. 2005, *Icarus*, 173, 108, doi: <https://doi.org/10.1016/j.icarus.2004.07.021>
- Pravec, P., Harris, A., Vokrouhlický, D., et al. 2008, *Icarus*, 197, 497, doi: <https://doi.org/10.1016/j.icarus.2008.05.012>
- Pál, A., Szakáts, R., Kiss, C., et al. 2020, *The Astrophysical Journal Supplement Series*, 247, 26, doi: [10.3847/1538-4365/ab64f0](https://doi.org/10.3847/1538-4365/ab64f0)
- Qian, Q., Yang, H., Zang, W., et al. 2025, *Publications of the Astronomical Society of the Pacific*, 137, 064401, doi: [10.1088/1538-3873/add9cf](https://doi.org/10.1088/1538-3873/add9cf)
- Tian, J., Zhao, H.-B., & Li, B. 2022, *Research in Astronomy and Astrophysics*, 22, 125004, doi: [10.1088/1674-4527/ac977d](https://doi.org/10.1088/1674-4527/ac977d)
- Vaduvescu, O., Macias, A. A., Tudor, V., et al. 2017, *Earth, Moon, and Planets*, 120, 41, doi: <https://doi.org/10.1007/s11038-017-9506-9>
- Vokrouhlický, D., Bottke, W., Chesley, S., Scheeres, D., & Statler, T. 2015, *Asteroids IV* (Tucson, AZ), Univ. Arizona Press, doi: [10.2458/azu_uapress_9780816532131-ch027](https://doi.org/10.2458/azu_uapress_9780816532131-ch027)
- Warner, B. D., & Harris, A. W. 2011, *Icarus*, 216, 610, doi: <https://doi.org/10.1016/j.icarus.2011.10.007>
- Warner, B. D., Harris, A. W., & Pravec, P. 2009, *Icarus*, 202, 134, doi: <https://doi.org/10.1016/j.icarus.2009.02.003>
- Waszczak, A., Chang, C.-K., Ofek, E. O., et al. 2015, *The Astronomical Journal*, 150, 75, doi: [10.1088/0004-6256/150/3/75](https://doi.org/10.1088/0004-6256/150/3/75)
- Xu, X., Wang, X., Muinonen, K., et al. 2023, *Monthly Notices of the Royal Astronomical Society*, 521, 3925, doi: [10.1093/mnras/stad765](https://doi.org/10.1093/mnras/stad765)
- Yang, H., Yee, J. C., Hwang, K.-H., et al. 2023, *Monthly Notices of the Royal Astronomical Society*, 528, 11, doi: [10.1093/mnras/stad3672](https://doi.org/10.1093/mnras/stad3672)
- Yang, H., Yee, J. C., Zhang, J., et al. 2025, *AJ*, 169, 295, doi: [10.3847/1538-3881/adc73e](https://doi.org/10.3847/1538-3881/adc73e)
- Yang, H., Zang, W., Valdes, F., et al. 2026, *arXiv e-prints*, arXiv:2605.27364, doi: [10.48550/arXiv.2605.27364](https://doi.org/10.48550/arXiv.2605.27364)
- Yeh, T.-S., Li, B., Chang, C.-K., et al. 2020, *The Astronomical Journal*, 160, 73, doi: [10.3847/1538-3881/ab9a32](https://doi.org/10.3847/1538-3881/ab9a32)
- Ďurech, J., Hanuš, J., Brož, M., et al. 2018, *Icarus*, 304, 101, doi: <https://doi.org/10.1016/j.icarus.2017.07.005>

APPENDIX

A. ASTEROIDS LIST

This appendix provides the derived rotation periods and associated parameters for the asteroid sample. Table 3 lists the reliable rotation period determinations ($U \geq 2+$), while Table 4 presents the less reliable rotation period determinations ($U < 2+$). Only asteroids with measurable rotation periods are included; objects for which no rotation period could be determined owing to insufficient data are excluded.

Table 3. List of reliable rotation periods. ^a Derived from the MPCORB database.

Object	Period (h)	Quality	H^a (mag)	Magnitude (I-band)	Amplitude (mag)	Epochs	<i>Phase Angle</i> ^a (°)
(1077) Campanula	3.8378 ± 0.0008	2+	12.36	15.407	0.4375	48	26.4939
(1152) Pawona	3.4348 ± 0.0004	2+	11.17	14.873	0.2216	83	24.4671
(1187) Afra	13.8938 ± 0.0119	2+	11.62	16.150	0.4563	47	21.0534
(1324) Knysna	2.5503 ± 0.0007	2+	13.20	15.548	0.1308	87	30.2324
(2294) Andronikov	3.1534 ± 0.0001	3-	11.91	14.925	0.4518	189	14.1802
(2438) Oleshko	3.2222 ± 0.0003	2+	13.02	15.660	0.2007	142	24.7712
(3180) Morgan	2.4481 ± 0.0004	3-	14.21	17.809	0.2003	200	22.0880
(3314) Beals	5.4650 ± 0.0039	2+	13.11	17.038	1.3315	24	23.7157
(4362) Carlisle	2.6320 ± 0.0002	2+	13.18	16.178	0.1878	170	24.5133
(5116) Korsor	4.5033 ± 0.0004	3	12.06	16.349	0.4812	114	2.2259
(6399) Harada	10.9662 ± 0.0002	3	13.04	16.226	1.2739	267	22.8387
(6690) Messick	3.0308 ± 0.0003	3-	13.68	14.568	0.2339	106	3.4887
(7284) 1989 VW	26.8283 ± 0.0549	2+	11.69	17.585	0.2260	191	6.0828
(10229) 1997 WR3	3.2508 ± 0.0004	3-	14.03	15.978	0.2766	166	11.4435
(12015) 1996 WA	5.2515 ± 0.0039	2+	15.00	17.755	0.1395	133	10.3298
(13564) Kodomomiraikan	2.9924 ± 0.0007	3-	15.00	17.501	0.3484	162	2.6714
(16673) 1994 BF1	3.1515 ± 0.0008	3-	14.37	17.234	0.2178	162	2.4585
(17039) Yeuseyenka	9.0525 ± 0.0118	2+	14.05	18.274	0.1753	126	21.2855
(17234) 2000 EL11	6.6400 ± 0.0002	3-	14.64	18.516	0.6868	332	11.6672
(17262) Winokur	6.4775 ± 0.0004	3-	14.71	18.286	0.2399	753	18.6021
(20753) 2000 AW211	6.1301 ± 0.0004	3-	13.83	17.599	1.0858	138	23.2769
(20917) 5016 P-L	54.4984 ± 0.1515	2+	15.42	17.602	0.3816	191	25.7187
(23444) Kukucin	8.5928 ± 0.0010	3	13.73	16.229	0.4395	170	22.6733
(23616) 1996 HY10	23.3896 ± 0.0244	2+	14.18	18.693	0.2901	291	18.3271
(27113) 1998 VY54	7.1788 ± 0.0087	3-	15.00	18.458	0.7787	61	27.2459
(28149) Arieldaniel	48.1271 ± 0.1530	2+	15.72	18.986	0.1814	316	19.6338
(29377) 1996 GV18	8.6125 ± 0.0012	3-	14.77	17.863	0.6702	323	13.4368
(31929) 2000 GF79	3.9052 ± 0.0062	2+	15.55	18.339	0.6843	31	33.8674
(34843) 2001 SZ276	3.0965 ± 0.0008	3-	14.69	17.730	0.3522	123	7.0559
(36342) 2000 NX15	10.6395 ± 0.0027	3-	15.50	19.487	0.6603	388	18.3337
(39414) 3283 T-1	8.5067 ± 0.0227	2+	15.85	19.128	0.2670	120	24.8223
(43749) 1981 EG46	5.6297 ± 0.0013	2+	16.07	18.721	0.1831	425	19.2054
(45119) 1999 XA86	5.2865 ± 0.0005	3-	13.05	16.681	0.4802	147	17.7351
(45711) 2000 FD43	3.3310 ± 0.0035	2+	14.53	18.892	0.3808	90	20.8770
(46339) 2001 RU81	4.1786 ± 0.0003	3	14.41	17.503	0.6991	178	9.5006
(48986) 1998 QJ47	4.9197 ± 0.0007	3-	15.06	17.411	0.8307	81	3.0105
(50739) Gracecook	7.7088 ± 0.0026	2+	13.89	16.782	0.4636	91	24.3527

Table 3. Continued.

Object	Period (h)	Quality	H^a (mag)	Magnitude (I-band)	Amplitude (mag)	Epochs	Phase Angle ^a (°)
(51905) 2001 QM51	19.4273 ± 0.1946	2+	14.65	18.339	0.3014	60	7.8539
(53834) 2000 ES179	17.4201 ± 0.0213	2+	15.07	16.487	0.2494	156	4.9848
(55585) 2002 PQ45	11.3697 ± 0.0007	3-	16.02	17.847	0.7716	185	7.5894
(58243) 1993 NG1	9.3101 ± 0.0007	2+	15.32	18.615	0.2318	287	15.8864
(58631) 1997 WE2	9.6653 ± 0.0109	2+	14.87	17.019	0.8775	45	8.0982
(59268) 1999 CU34	44.7391 ± 0.0800	2+	15.10	18.512	0.2640	326	19.4154
(68155) 2001 BM9	5.9969 ± 0.0077	2+	15.51	18.741	0.3538	110	26.8556
(70818) 1999 VJ77	5.3952 ± 0.0027	2+	15.27	19.161	0.3914	219	12.5757
(71628) 2000 EJ69	3.6411 ± 0.0006	2+	14.20	19.553	0.2034	652	14.3664
(74164) 1998 QL104	4.6043 ± 0.0026	2+	15.65	18.642	0.3799	133	23.5719
(74179) 1998 RZ23	5.4627 ± 0.0042	3	15.55	18.259	0.8135	60	30.2836
(74455) 1999 CW28	3.8223 ± 0.0010	3-	14.55	18.503	0.6268	190	2.1568
(77143) 2001 EN3	49.0609 ± 0.1328	2+	16.88	18.812	0.2190	555	18.5822
(80017) 1999 GQ39	13.7048 ± 0.0087	2+	15.16	17.809	0.3048	236	17.2110
(81055) 2000 EJ65	39.0776 ± 0.0024	2+	15.37	18.736	1.2282	110	25.5256
(81146) 2000 EW142	13.7950 ± 0.0513	2+	15.52	19.475	0.7600	53	26.5698
(82123) 2001 FY77	46.8159 ± 0.0094	2+	15.64	17.521	0.1841	228	16.9608
(83278) 2001 RQ84	3.3259 ± 0.0012	3-	15.36	17.914	0.2819	139	4.0799
(84674) 2002 VT87	5.5964 ± 0.0108	2+	15.54	19.219	0.2681	183	1.9749
(84964) 2003 YF14	14.4092 ± 0.0148	2+	15.16	18.785	0.2188	302	15.8500
(87265) 2000 OL58	47.4877 ± 0.2020	2+	15.03	18.929	0.3220	214	20.0696
(89573) 2001 XD118	6.0378 ± 0.0011	2+	15.78	18.628	0.7110	206	15.6900
(94431) 2001 TZ41	4.7054 ± 0.0024	2+	15.80	19.183	0.2722	229	16.4916
(97595) 2000 EX37	49.1708 ± 0.3245	2+	14.38	18.478	0.2023	281	10.5501
(98355) 2000 SZ335	2.5911 ± 0.0014	2+	15.43	17.968	0.2388	95	8.4357
(100945) 1998 OE8	9.7430 ± 0.0002	3-	16.23	18.463	0.9910	123	17.5123
(101221) 1998 SB62	6.1311 ± 0.0002	2+	16.20	18.629	0.5877	174	13.4155
(103266) 2000 AT26	13.5153 ± 0.0072	3-	14.66	18.430	0.7134	210	3.1524
(105939) 2000 SY227	9.1709 ± 0.0004	3	16.13	18.143	0.7499	182	10.4101
(107095) 2001 AA30	7.9434 ± 0.0262	2+	16.11	18.877	0.2249	111	3.4438
(107806) 2001 FZ58	6.9973 ± 0.0020	3	15.85	17.312	0.6329	91	6.6548
(108332) 2001 KP2	3.5687 ± 0.0037	2+	16.10	18.884	1.1915	30	35.9095
(116375) 2003 YU111	11.4796 ± 0.0084	3-	14.78	19.044	0.8060	223	4.3588
(117092) 2004 NB7	5.5600 ± 0.0002	3-	15.20	18.333	0.4220	228	11.6151
(127443) 2002 PX69	3.0104 ± 0.0005	3-	14.58	17.716	0.2525	255	9.9252
(128072) 2003 OV9	2.4736 ± 0.0012	2+	15.06	18.256	0.1525	224	6.0009
(136881) 1998 FL133	10.5715 ± 0.0048	3-	16.90	18.237	0.7585	144	8.7321
(141541) 2002 GL14	10.5601 ± 0.0003	2+	16.72	18.952	0.9825	102	25.5147
(148858) 2001 VH56	15.7087 ± 0.0819	2+	15.49	18.775	0.2896	107	2.4846
(149647) 2004 FC38	12.4895 ± 0.0283	2+	16.75	18.767	0.3547	138	7.9643
(201332) 2002 TV160	3.4291 ± 0.0017	3-	14.90	17.480	0.2505	62	2.8104
(208317) 2001 MF3	6.2835 ± 0.0082	2+	16.61	18.207	0.2616	147	8.7252
(211013) 2001 YK33	5.6454 ± 0.0045	2+	16.21	19.290	0.5907	86	2.4928
(217434) 2005 SY95	5.9390 ± 0.0030	3-	15.77	18.345	0.5383	138	10.6327
(251421) 2008 AR81	11.8864 ± 0.0245	2+	16.55	19.014	0.4151	136	7.2758
(252478) 2001 UY44	3.5498 ± 0.0001	2+	16.11	18.837	0.4019	176	10.2614

Table 3. Continued.

Object	Period (h)	Quality	H^a (mag)	Magnitude (I-band)	Amplitude (mag)	Epochs	$Phase\ Angle^a$ ($^\circ$)
(283926) 2004 NT8	13.6128 ± 0.0078	2+	17.55	19.102	0.2815	360	23.0960
(306902) 2001 TV171	3.1264 ± 0.0014	2+	16.65	18.394	0.2426	128	17.9808
(307441) 2002 UQ28	100.3625 ± 0.4320	2+	14.57	19.264	0.6446	242	18.3822
(307779) 2003 WK64	59.4284 ± 0.5341	2+	16.50	19.309	0.9659	137	11.3891
(367941) 2012 DZ12	5.7286 ± 0.0035	2+	16.27	18.421	0.4193	104	3.3783
(394438) 2007 PJ35	30.5142 ± 0.1717	2+	17.32	18.433	0.2350	157	13.1460
(400148) 2006 UT288	5.5949 ± 0.0048	2+	16.50	18.953	0.5920	66	5.4733
(434102) 2002 JY100	5.2161 ± 0.0159	3-	17.93	18.609	0.4315	52	4.8421
(639562) 2017 FD53	5.4108 ± 0.0007	3-	15.13	18.944	0.4859	305	19.1602
(661761) 2005 NT79	15.6609 ± 0.0855	2+	18.51	19.054	0.6273	66	3.7807
(666079) 2009 WM173	9.3606 ± 0.0099	2+	15.63	18.593	0.8881	84	7.0842
(700192) 2000 ED211	9.4238 ± 0.0064	3-	16.24	19.225	0.5297	196	7.9677
(742117) 2007 CB84	5.1335 ± 0.0093	2+	17.51	19.398	0.8952	30	5.0937

Table 4. List of less reliable rotation periods. ^a Derived from the MPCORB database.

Object	Period (h)	Quality	H^a (mag)	Magnitude (I-band)	Amplitude (mag)	Epochs	Phase ($^\circ$)
(2472) Bradman	56.2092 ± 0.3750	2-	14.0	17.353	0.3283	77	25.3814
(2899) Runrun Shaw	23.7101 ± 0.0198	1+	13.57	14.911	0.2438	183	9.6227
(9764) Morgenstern	12.4226 ± 0.0040	2-	14.56	17.567	0.1373	171	5.7014
(15699) Lyytinen	2.3682 ± 0.0012	2-	14.62	17.670	0.1174	66	6.8504
(18877) Stevendodds	44.9685 ± 0.0382	2	13.71	18.318	0.1152	381	15.0026
(19734) 1999 XE175	47.8534 ± 0.1026	2	14.2	18.946	0.1889	582	15.2399
(27215) 1999 CK128	26.9112 ± 0.1636	2-	13.99	17.96	0.3624	59	11.8447
(28165) Bayanmashat	13.7013 ± 0.0164	2-	14.9	18.024	1.1257	64	28.9287
(30818) 1990 RH2	46.1798 ± 0.0951	2	15.31	18.914	0.2327	134	24.9217
(31939) Thananon	69.8331 ± 0.0037	2	14.81	16.815	0.5612	140	20.2091
(32357) 2000 QR124	51.6199 ± 0.6893	1+	15.15	18.595	0.3553	73	25.0919
(33062) 1997 VT2	36.5535 ± 0.4157	1+	15.28	17.503	0.2532	69	8.1180
(35523) 1998 FQ63	50.9474 ± 0.6100	1+	14.18	17.817	0.2690	73	24.9356
(36932) 2000 SK221	13.3921 ± 0.0829	2-	14.27	19.267	0.7117	49	19.5345
(37108) 2000 UG102	72.0379 ± 0.5290	1+	15.12	17.785	0.1940	200	6.5183
(39085) 2000 VW34	59.5706 ± 0.8246	1+	14.3	18.426	0.4069	123	9.5215
(42287) 2001 TE51	44.0706 ± 0.2008	2-	15.66	17.423	0.2429	118	7.5268
(43325) 2000 KY50	46.9862 ± 0.2692	2-	14.06	16.457	0.3212	57	4.6746
(43562) 2001 FE97	76.5544 ± 0.4930	2	14.02	18.288	0.4266	142	14.9578
(45394) 2000 AO132	39.3431 ± 0.3160	1+	14.27	18.905	0.1613	133	18.9285
(46980) 1998 SW156	18.2270 ± 0.0009	1+	14.84	18.262	0.7326	98	24.2534
(47664) 2000 CE54	180.0741 ± 0.7711	1+	13.59	16.823	0.6819	175	3.1813
(47690) 2000 CQ92	15.5726 ± 0.0365	1	14.18	18.705	0.7098	82	9.3349
(48867) 1998 HR67	13.6249 ± 0.0892	2	14.99	17.5	0.2318	57	30.1097
(50006) 2000 AY19	53.1549 ± 0.6756	1+	15.15	18.564	0.2835	115	26.1825
(50783) 2000 FE17	124.3644 ± 0.5744	2-	14.9	18.595	0.7914	223	11.0326
(51256) 2000 JB58	49.1065 ± 0.3104	2-	14.52	17.594	0.1730	179	10.8052
(54877) 2001 OU51	24.4071 ± 0.2212	2	15.23	18.715	0.3978	65	26.4843
(56126) 1999 CT31	14.3987 ± 0.0023	2	15.21	17.702	0.1569	227	9.3990
(56447) 2000 GR76	51.2280 ± 0.3813	2	16.07	18.888	0.7592	125	16.5030
(57171) 2001 QT20	50.8154 ± 0.1933	2	15.46	18.107	0.2655	158	16.2304
(58261) 1993 SD1	16.9603 ± 0.0578	1+	15.0	17.231	0.1017	148	8.3756
(58586) 1997 SG23	43.9946 ± 0.1133	2-	15.62	18.831	0.6461	74	23.4172
(59292) 1999 CN56	24.0643 ± 0.0325	2-	15.09	18.414	0.1178	505	19.5274
(62476) 2000 SH219	52.3341 ± 0.7510	2-	14.17	19.048	0.6768	51	21.2614
(66426) 1999 NW33	29.5877 ± 0.2598	2-	15.33	18.639	0.2122	84	28.0022
(66950) 1999 XQ11	21.9396 ± 0.2319	2-	14.43	18.304	0.2556	101	7.7834
(71588) 2000 DK68	23.0660 ± 0.1926	2-	14.51	18.772	0.6749	73	3.7874
(72747) 2001 FR121	4.7434 ± 0.0005	2	14.17	18.279	0.1064	713	17.2128
(72855) 2001 HX43	17.5550 ± 0.1220	2-	14.77	18.952	0.6906	63	12.7518
(76868) 2000 YC11	53.5829 ± 0.5000	1+	15.46	17.81	0.2665	81	29.9274
(77602) 2001 KZ26	67.3999 ± 0.4939	2-	14.94	17.842	0.2192	160	21.2950
(77684) 2001 NO	208.5826 ± 0.9087	1+	15.2	17.331	2.3970	117	2.9159
(78743) 2002 TZ273	36.5630 ± 0.6716	2-	14.43	18.145	0.3937	43	3.5201
(79538) 1998 QN34	23.9277 ± 0.0470	2-	15.65	17.756	0.2928	142	23.5240

Table 4. Continued.

Object	Period (h)	Quality	H^a (mag)	Magnitude (I-band)	Amplitude (mag)	Epochs (au)	Phase ($^\circ$)
(80144) 1999 TY124	13.5813 ± 0.0638	2-	16.56	18.816	0.2785	94	5.3624
(86857) 2000 HW9	20.6596 ± 0.1916	1+	15.86	17.691	0.1084	176	8.2107
(86979) 2000 JW19	46.0559 ± 0.6352	1+	15.58	18.532	0.2500	136	25.7173
(88348) 2001 OT75	3.3026 ± 0.0045	2	16.36	19.611	0.3100	139	24.6681
(88607) 2001 QE296	46.0567 ± 0.2387	1+	16.47	16.977	0.3040	74	8.9281
(89019) 2001 TC90	36.9515 ± 0.3346	2-	15.13	19.126	0.5542	92	23.3249
(89691) 2001 YC70	51.9042 ± 0.1057	2	16.07	18.92	0.2358	311	16.3178
(89720) 2001 YQ122	84.1470 ± 0.1498	2-	15.36	16.966	0.8038	175	9.1279
(90614) 6646 P-L	25.1947 ± 0.1016	1	15.1	18.471	0.4017	156	4.7730
(97617) 2000 EW104	48.9426 ± 0.5383	1+	13.86	18.28	0.3785	53	21.8038
(97968) 2000 QT149	460.3904 ± 0.8444	1+	16.28	18.565	1.1542	156	13.4797
(98436) 2000 UF42	41.0651 ± 0.4535	2-	15.54	18.589	0.1273	219	9.9560
(100728) Kamenice n Lipou	93.3757 ± 0.8197	1+	15.92	19.215	0.7432	118	5.0539
(101187) 1998 SV13	31.1032 ± 0.5827	2-	16.12	19.133	0.3628	54	5.6327
(101486) 1998 WJ38	82.0681 ± 0.8385	1+	15.23	19.29	0.4666	122	1.9485
(101649) 1999 CO62	16.7503 ± 0.1015	2	13.66	19.098	0.3991	66	16.3625
(102237) 1999 TQ21	5.1312 ± 0.0073	2-	15.01	19.503	0.2557	114	9.3657
(103250) 2000 AY6	53.3729 ± 0.7454	1	14.96	17.736	0.2066	86	5.9229
(104270) 2000 EC149	56.2806 ± 0.5053	2-	16.31	18.761	0.3996	166	2.5179
(108042) 2001 FG155	50.6397 ± 0.5122	2-	16.84	17.708	0.2196	83	7.4255
(108149) 2001 HG2	21.9927 ± 0.3784	1+	15.91	19.257	0.4407	57	28.1275
(110835) 2001 UA65	83.3481 ± 0.5373	2-	15.15	18.326	0.3320	163	8.1478
(113697) 2002 TM121	47.6207 ± 0.0372	2-	16.44	18.768	0.3576	174	12.4105
(113901) 2002 TX274	8.5787 ± 0.0439	2-	16.91	19.106	0.3682	72	16.8859
(115599) 2003 UJ99	48.9481 ± 0.7319	1+	15.11	17.146	0.2059	65	7.4849
(119256) 2001 RW28	5.3012 ± 0.0816	1+	15.89	18.759	0.1635	89	2.5528
(124358) 2001 QA131	20.7772 ± 0.3458	1	16.17	19.193	0.3409	63	25.6011
(142389) 2002 SQ11	27.8556 ± 0.5270	2	16.32	19.807	0.2154	121	23.1698
(145499) 2006 BV33	59.6000 ± 0.7891	1	15.38	18.178	0.2209	93	2.9077
(146337) 2001 OW14	30.4319 ± 0.4747	2	14.75	18.466	0.4706	67	25.7849
(147455) 2004 BK20	28.7172 ± 0.3066	2-	16.57	18.44	0.2121	145	2.7659
(149456) 2003 DA13	149.6609 ± 0.7822	1+	15.65	18.727	0.6662	176	9.3988
(153030) 2000 PV1	62.2428 ± 0.7463	2-	14.73	19.4	0.3223	121	7.2885
(153370) 2001 QU7	100.3049 ± 0.6155	1+	16.5	18.578	0.3416	153	13.3888
(153401) 2001 QG119	64.6498 ± 0.1424	1+	16.37	18.078	0.1519	262	8.7915
(154315) 2002 VO20	10.7503 ± 0.0585	2-	16.84	19.388	0.2310	108	5.9875
(154669) 2004 FA127	47.8187 ± 0.2481	2	17.11	18.028	0.2288	208	3.1640
(171188) 2005 JR20	46.3577 ± 0.7724	1	15.69	18.979	0.4701	86	24.4399
(173817) 2001 SU305	47.7476 ± 0.1773	1+	15.96	18.635	0.6862	188	7.7918
(180213) 2003 UM8	44.0264 ± 0.3784	2	17.03	18.643	0.2148	147	12.7505
(187043) 2005 KE12	32.8428 ± 0.1473	2	17.09	17.983	0.1566	141	29.1229
(192583) 1999 AY9	69.2668 ± 0.7715	1+	17.34	18.704	0.2476	89	10.2077
(196021) 2002 ST2	35.6629 ± 0.6409	1+	16.07	18.264	0.7812	67	17.8138
(197627) 2004 KO	66.1513 ± 0.2014	1+	17.75	19.467	0.2510	151	16.2388
(217474) 2005 WP113	48.5248 ± 0.6076	2-	16.07	18.368	0.2684	76	11.2875
(220436) 2003 UO283	49.8860 ± 0.7651	1+	17.01	19.034	0.1780	157	2.6949

Table 4. Continued.

Object	Period (h)	Quality	H^a (mag)	Magnitude (I-band)	Amplitude (mag)	Epochs (au)	Phase ($^\circ$)
(223998) 2005 EN324	47.6260 \pm 0.1627	2	17.68	18.825	0.2027	415	18.5846
(226525) 2003 UF98	63.1282 \pm 0.6991	1+	15.01	18.526	0.4649	122	10.3969
(228737) 2002 TB211	44.2943 \pm 0.4023	2-	16.79	19.226	0.3984	183	12.0934
(242994) 2006 SX412	43.3321 \pm 0.6401	1+	15.74	17.707	0.2080	98	3.0360
(246823) 2009 TO35	2.7887 \pm 0.0034	2	14.89	18.624	0.1364	161	8.1242
(248294) 2005 LZ2	11.5238 \pm 0.0813	2	16.11	18.947	0.4985	67	25.4408
(249205) 2008 DT39	50.8843 \pm 0.5408	1	16.19	19.475	0.5588	136	5.6187
(254797) 2005 QO86	47.8117 \pm 0.6782	1+	16.07	18.556	0.2939	100	6.0095
(259541) 2003 UW83	13.2512 \pm 0.0972	1	14.95	17.97	0.3462	60	5.0465
(270596) 2002 NS15	46.0932 \pm 0.7192	2	15.52	18.867	0.1610	163	10.6732
(272067) 2005 EK215	2.1530 \pm 0.0043	2	18.24	19.063	0.1422	55	3.8758
(285800) 2000 XG19	39.5676 \pm 0.6672	2-	16.23	19.38	0.1962	129	2.1635
(290837) 2005 WO14	49.2187 \pm 0.6318	2	16.64	19.243	0.3553	152	6.1133
(301922) 1999 VH159	19.0213 \pm 0.0956	1+	16.06	18.856	0.5001	119	4.9312
(306308) 2011 SL70	13.4124 \pm 0.0940	2-	17.57	19.317	0.2673	98	8.6754
(307829) 2003 YB26	76.9895 \pm 0.7886	1+	17.03	18.972	1.1297	117	14.1466
(307847) 2003 YN130	3.3822 \pm 0.0108	2	15.98	19.233	0.3338	61	6.8430
(310997) 2003 WT141	16.9212 \pm 0.6872	1+	17.33	18.744	0.4069	57	5.4341
(311000) 2003 WT157	77.7589 \pm 0.8922	1	17.4	19.074	40.8378	57	10.3563
(312702) 2010 OD87	61.8052 \pm 0.7163	2	16.15	18.634	0.3475	120	26.9363
(344511) 2002 RG85	38.9077 \pm 0.3209	2-	17.8	19.176	0.1222	179	14.0266
(387562) 2001 SL15	70.0307 \pm 0.8144	1+	17.63	18.623	0.1767	111	3.5966
(413291) 2003 UO164	17.5443 \pm 0.0915	2-	15.37	18.89	0.4100	85	2.2635
(415204) 2012 HZ14	28.2020 \pm 0.7051	1	16.14	19.033	0.1880	170	2.4885
(442649) 2012 TU124	58.3536 \pm 0.5590	1	18.05	18.228	0.2387	171	15.4212
(443402) 2014 HU37	44.7353 \pm 0.7058	1+	16.79	18.624	0.6685	69	6.6857
(547337) 2010 LF65	30.5449 \pm 0.6248	2	16.68	19.58	0.7176	57	6.5381
(565258) 2017 DG1	2.3137 \pm 0.0026	2	17.04	18.56	0.4057	64	34.3100
(573142) 2008 YK11	25.5075 \pm 0.1804	2	17.57	18.989	0.7353	74	2.9745
(614054) 2008 SC29	56.8403 \pm 0.6984	2-	18.37	19.109	0.2579	162	7.5052
(739003) 2017 DG118	102.0560 \pm 0.8148	1+	15.89	18.619	1.0100	96	2.7268
(829373) 2006 OB40	48.3685 \pm 0.5001	2-	17.46	19.049	0.2747	226	7.3110
(855712) 2011 GK57	59.7218 \pm 0.7456	1	18.59	18.974	0.2569	105	10.8725

B. LIGHTCURVE FIGURES

This appendix presents the folded light curves and the corresponding normalized χ^2 distributions as a function of frequency for asteroids with different rotation-period quality codes. Figures 8, Figures 9 and Figures 10 show the results for asteroids with $U = 3$, $U = 3-$, and $U = 2+$, respectively.

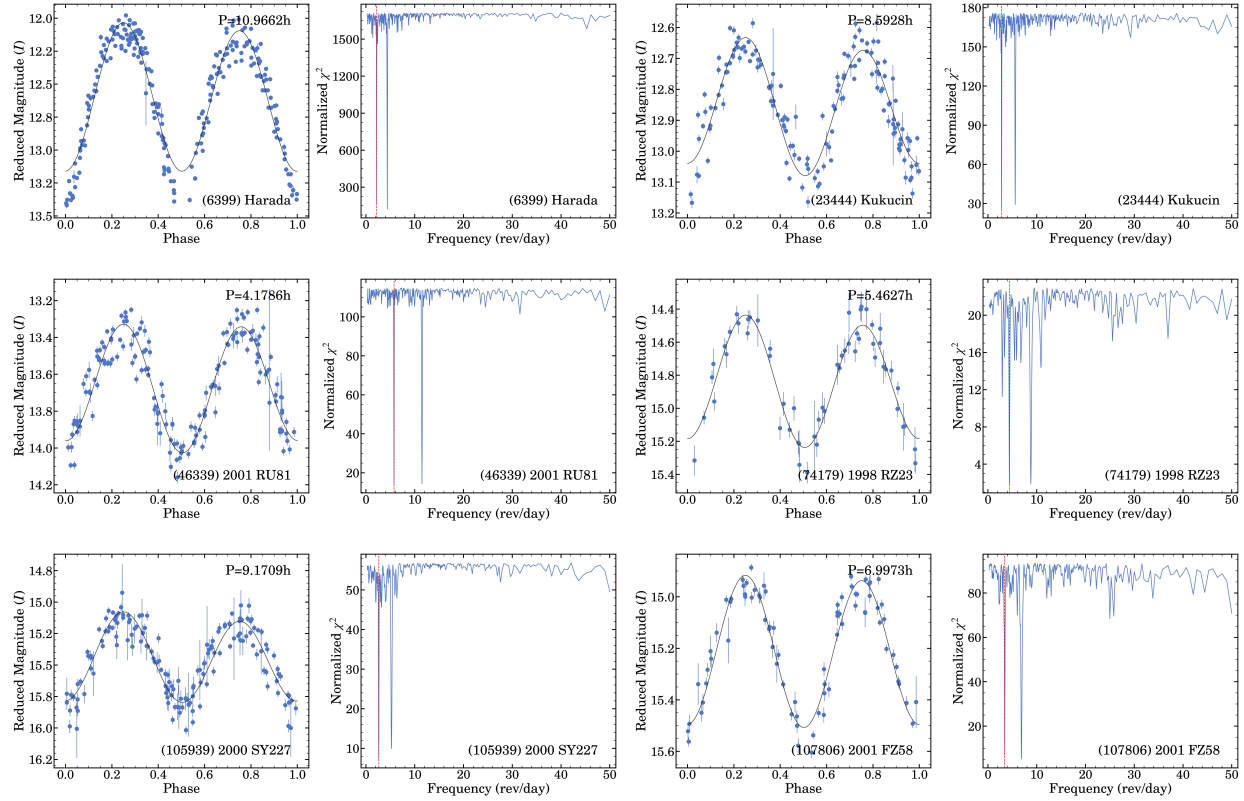


Figure 8. Folded lightcurves (left) and normalized χ^2 as a function of frequency (right) for asteroids with rotation period quality code $U = 3$.

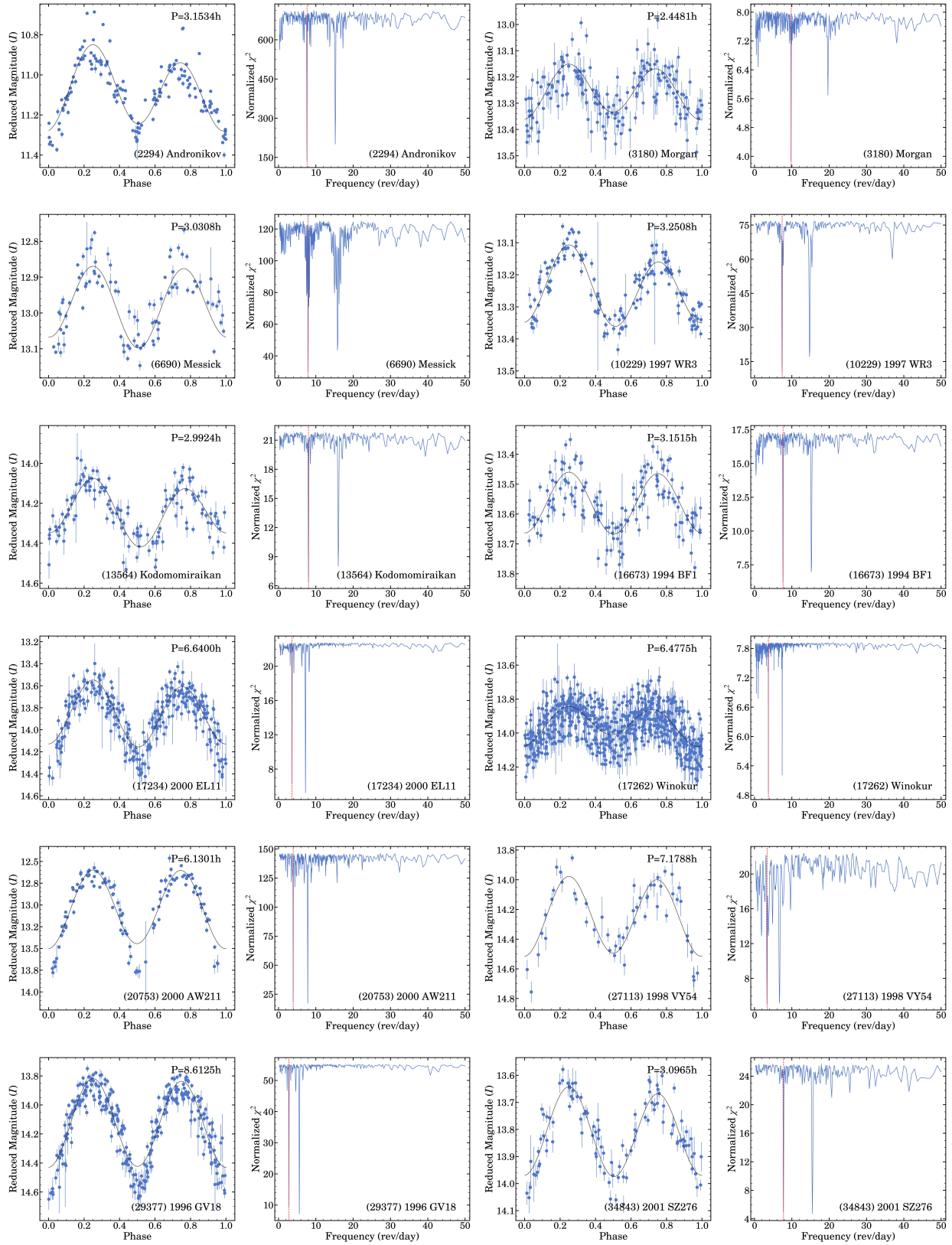
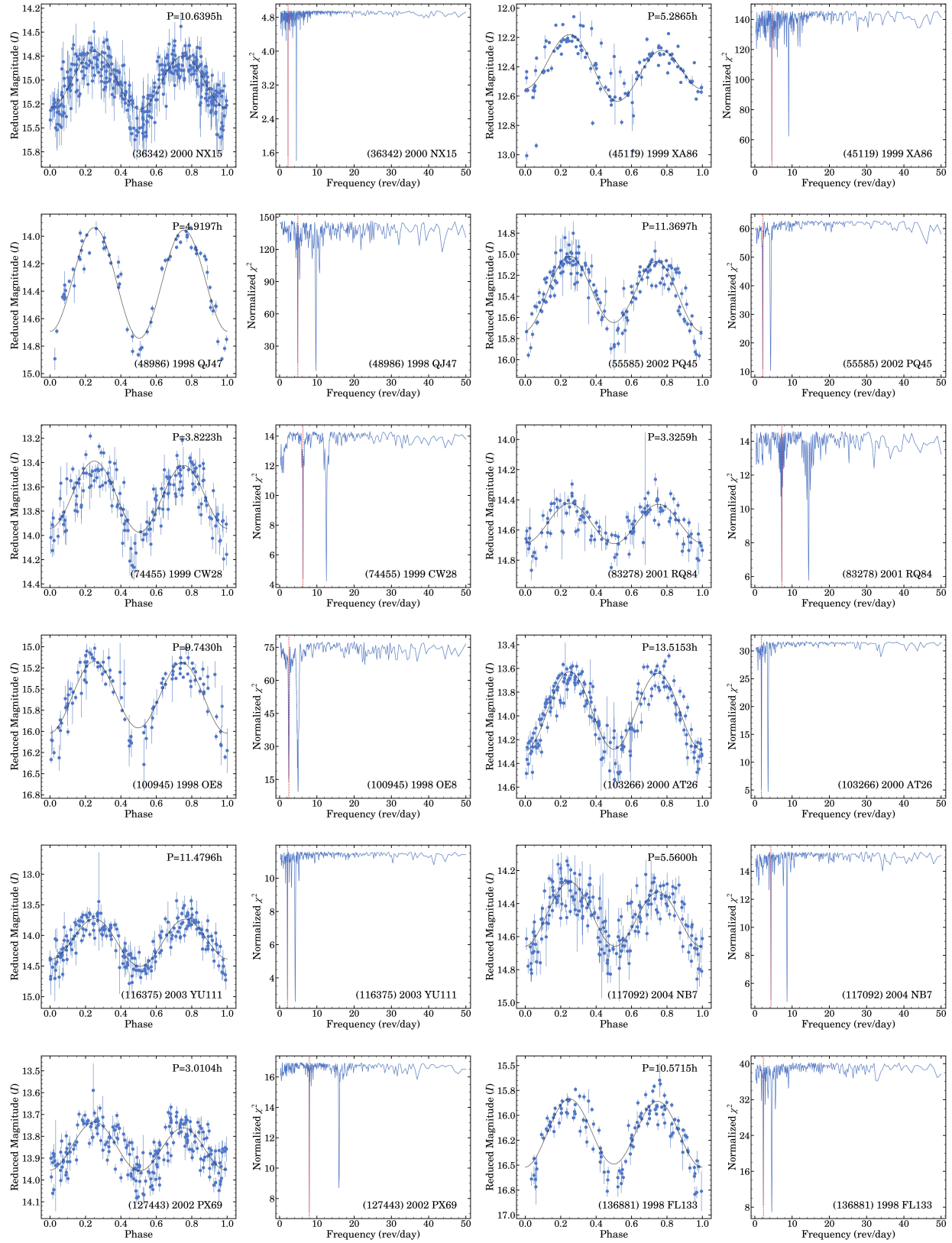


Figure 9. Folded lightcurves (left) and normalized χ^2 as a function of frequency (right) for asteroids with rotation period quality code U = 3-.

Figure 9. Continued ($U = 3-$).

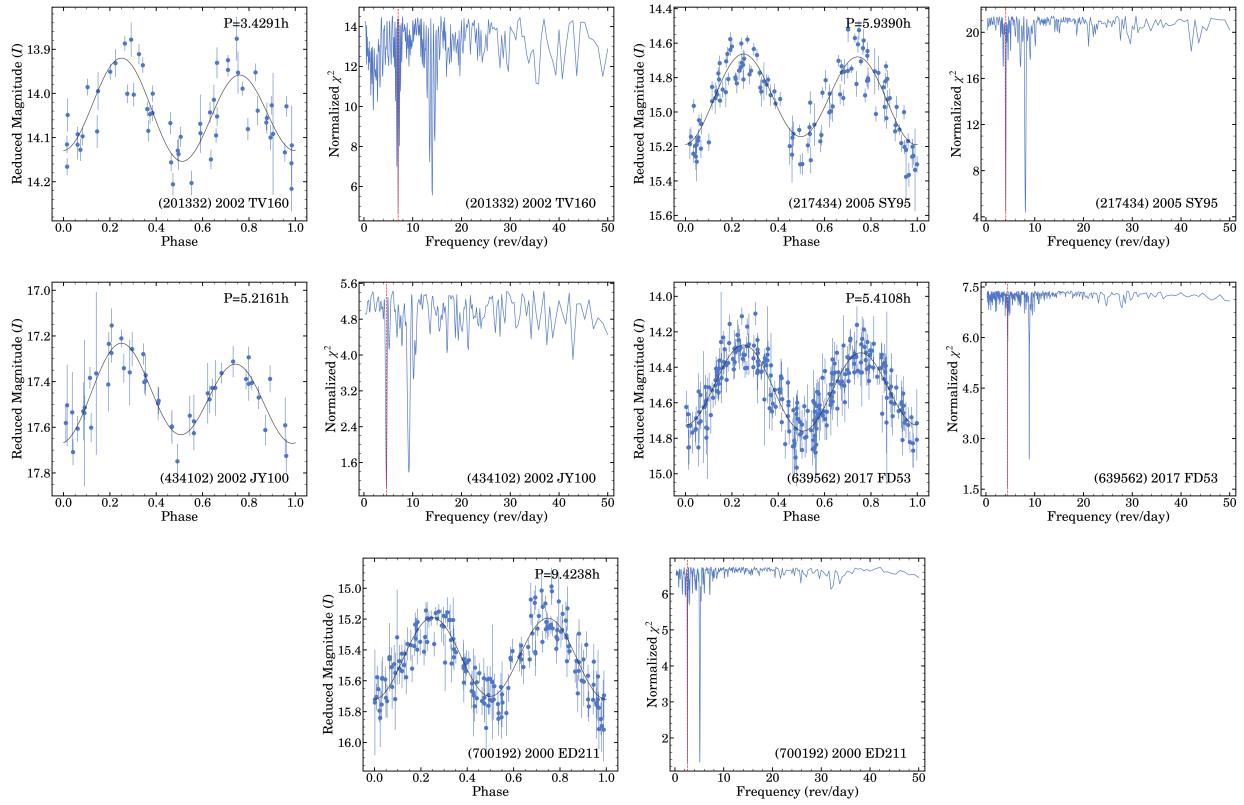


Figure 9. Continued ($U = 3-$).

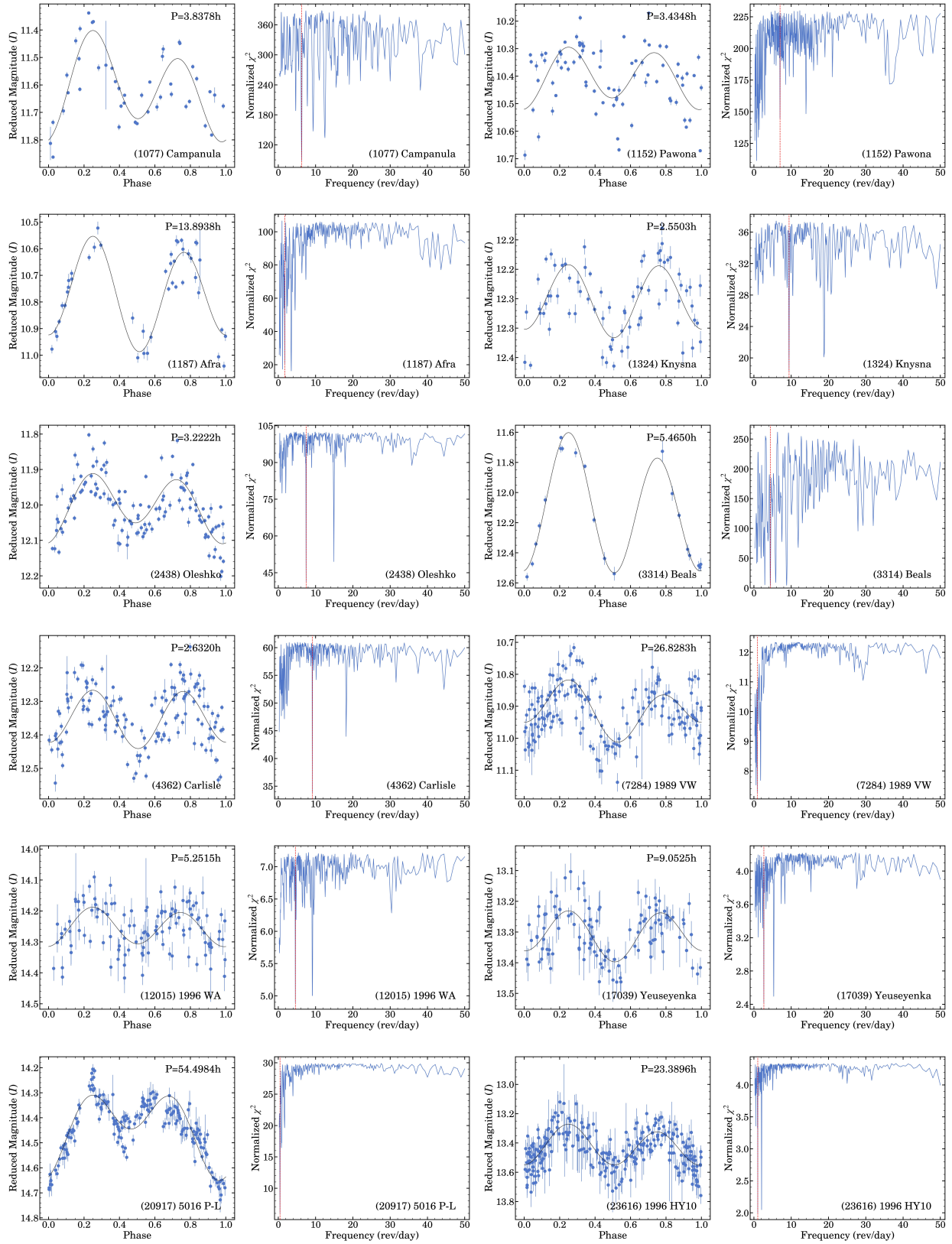


Figure 10. Folded lightcurves (left) and normalized χ^2 as a function of frequency (right) for asteroids with rotation period quality code $U = 2+$.

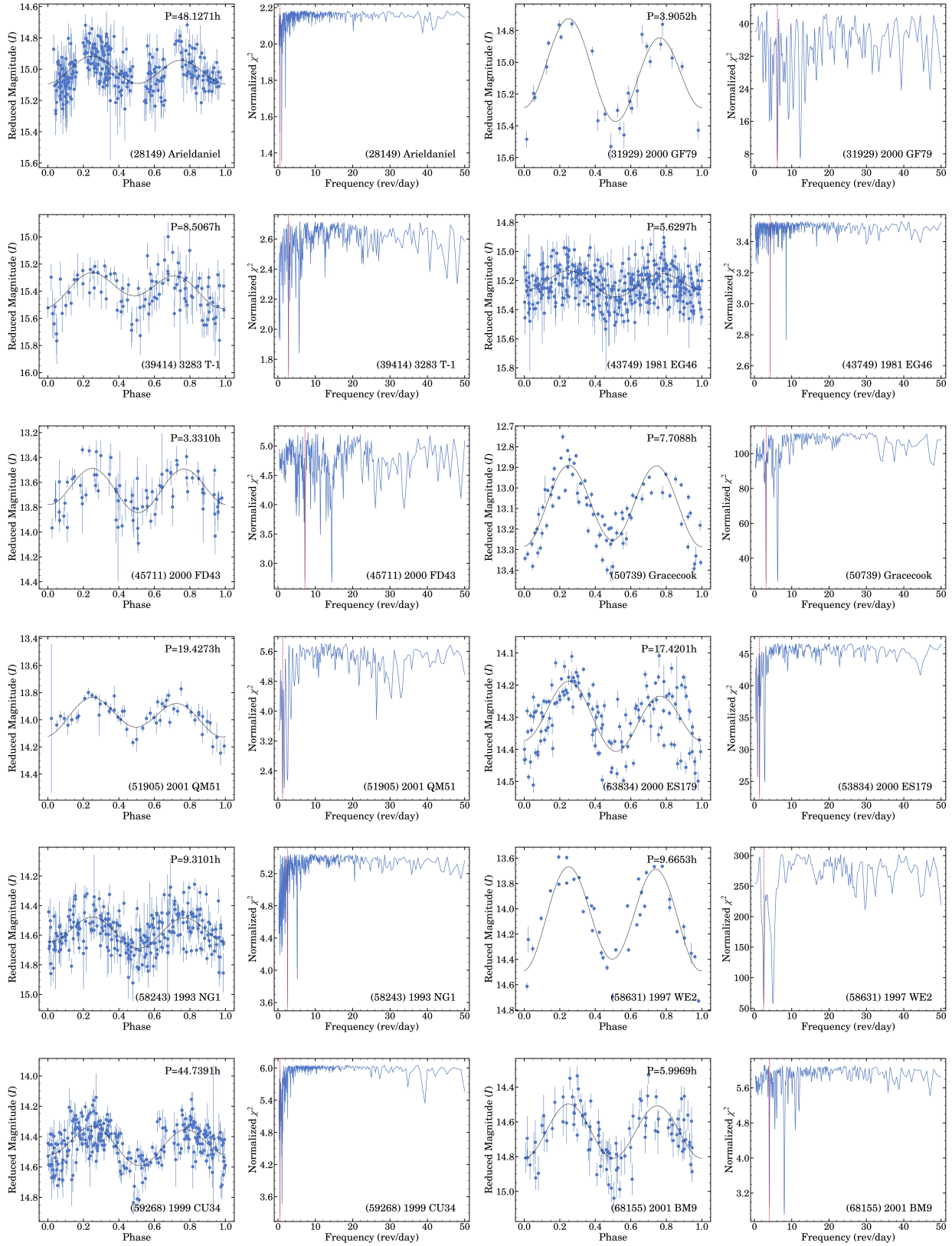
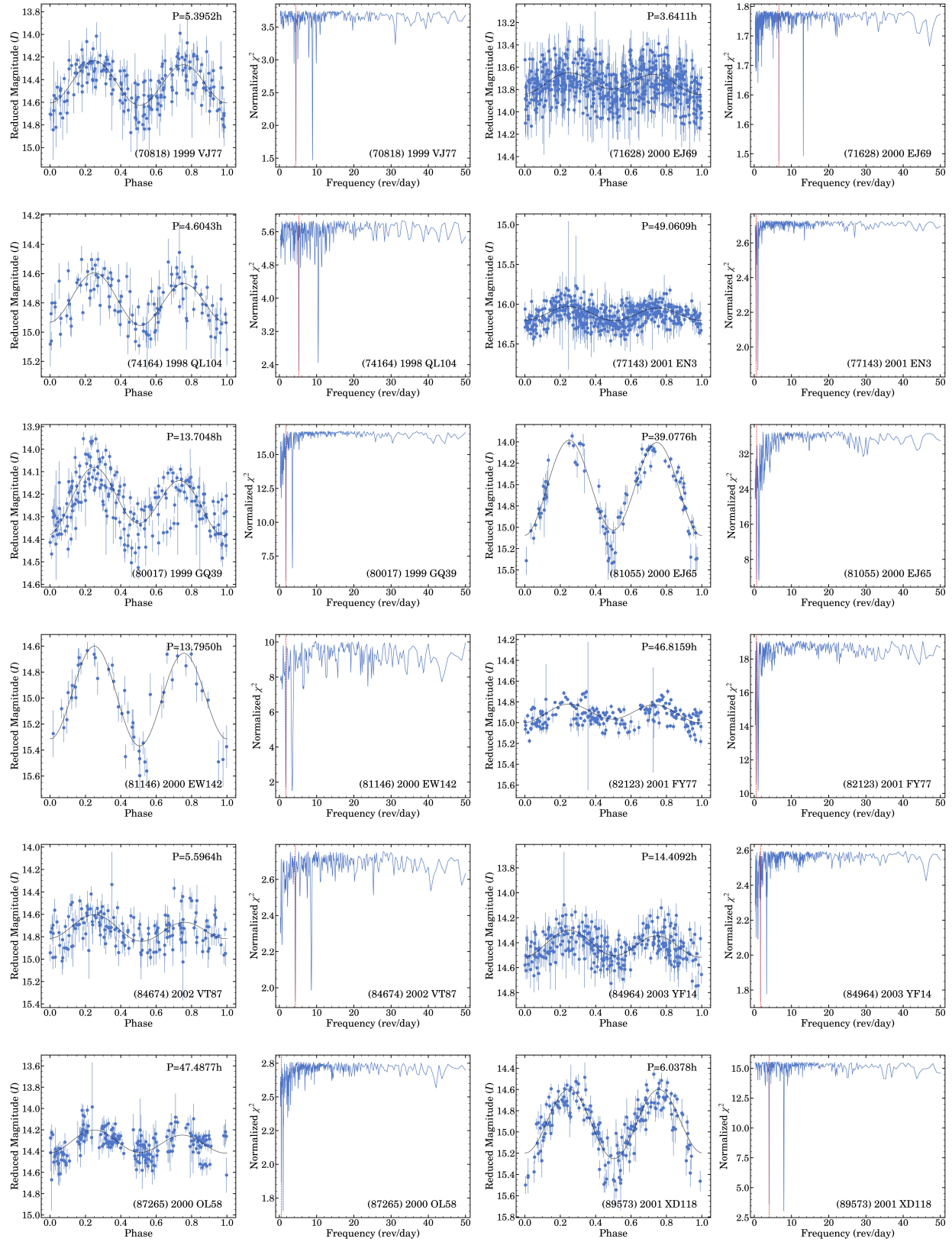


Figure 10. Continued ($U = 2+$).

Figure 10. Continued ($U = 2+$).

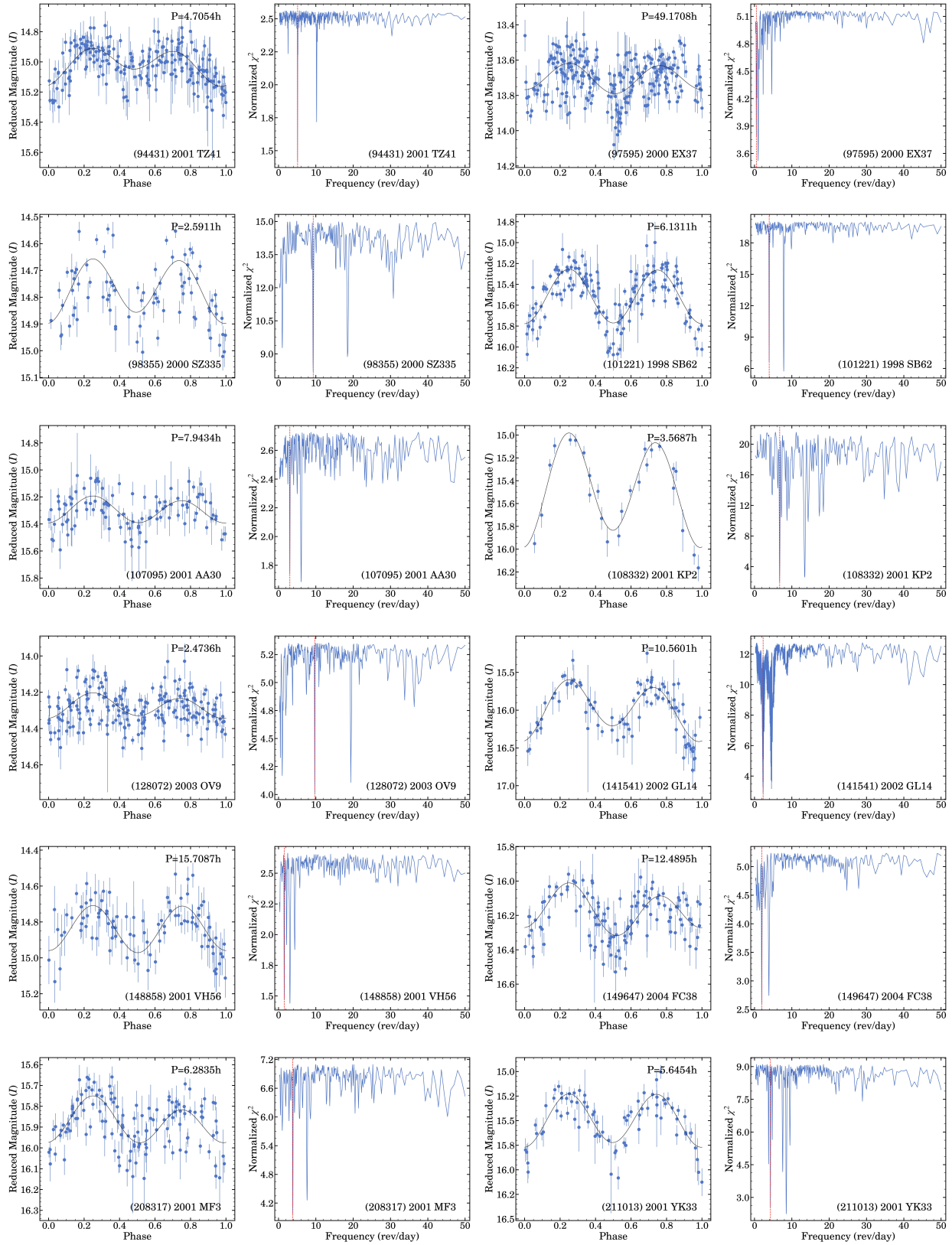
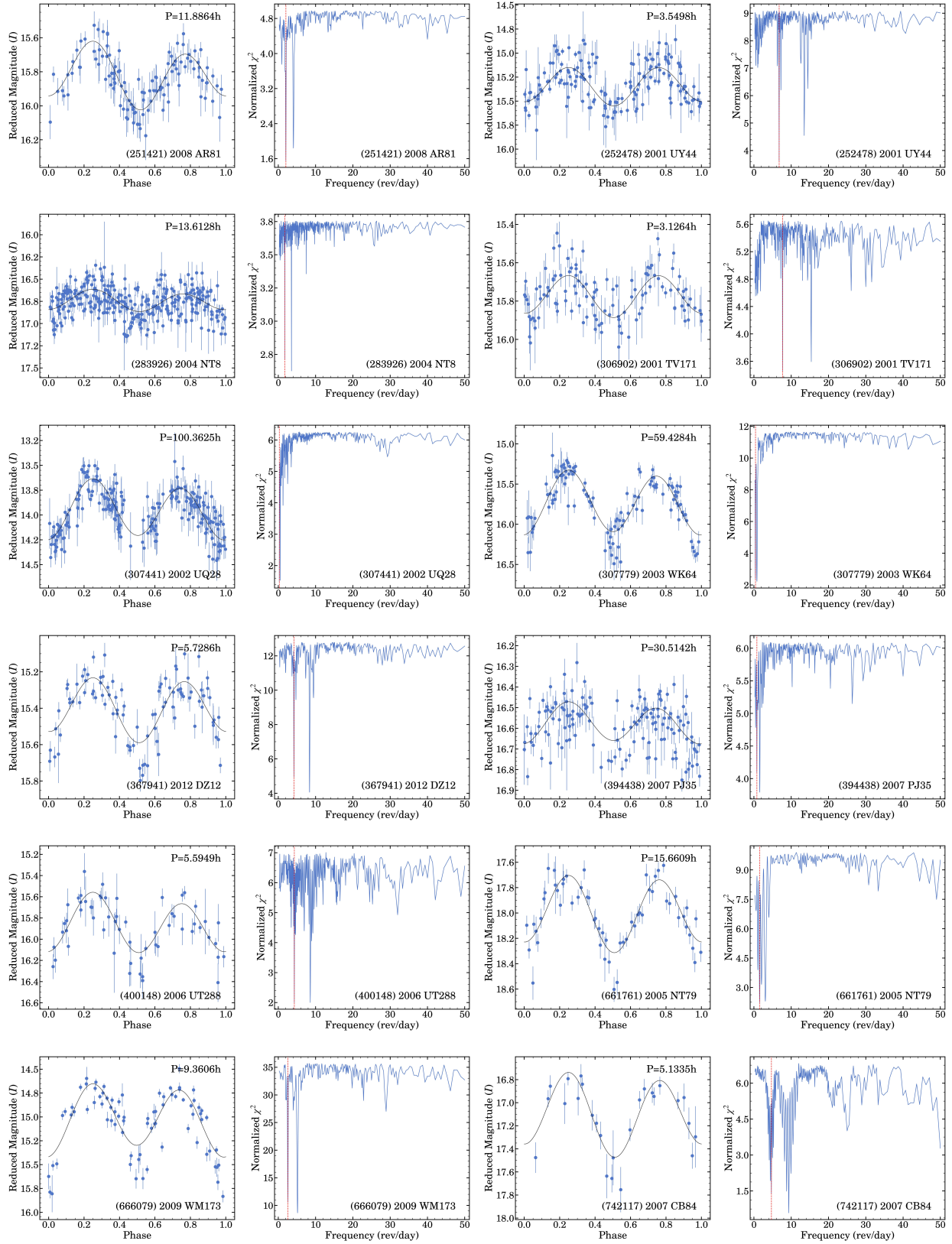


Figure 10. Continued ($U = 2+$).

Figure 10. Continued ($U = 2+$).